

# Nonperturbative Nonlinear Hall Effect in Nonequilibrium Steady States

Lei Geng,<sup>1,\*</sup> Martin Eckstein,<sup>2,3</sup> Lei Chen,<sup>4,5</sup> Shouvik Sur,<sup>4</sup> Silke Paschen,<sup>6</sup> Qimiao Si,<sup>4</sup> and Philipp Werner<sup>1,†</sup>

<sup>1</sup>*Department of Physics, University of Fribourg, Fribourg-1700, Switzerland*

<sup>2</sup>*Institute of Theoretical Physics, University of Hamburg, 20355 Hamburg, Germany*

<sup>3</sup>*The Hamburg Centre for Ultrafast Imaging, Hamburg, Germany*

<sup>4</sup>*Department of Physics and Astronomy, Extreme Quantum Materials Alliance, Smalley-Curl Institute, Rice University, Houston, Texas 77005, USA*

<sup>5</sup>*Department of Physics and Astronomy, Stony Brook University, Stony Brook, New York 11794, USA*

<sup>6</sup>*Institute of Solid State Physics, TU Wien, 1040 Vienna, Austria*

(Dated: July 3, 2026)

The nonlinear Hall effect in quantum materials has attracted broad interest, yet most existing studies focus on the weak-field, perturbative regime. Here we develop a nonperturbative approach based on nonequilibrium steady-state Green's functions for dc-field-driven lattice systems, with dissipation and interactions incorporated through self-energies beyond the constant relaxation-time approximation and interband transitions treated alongside their intraband counterparts. Applied to a two-band semimetal model, our approach provides direct access to the strong-field Hall response beyond the nonperturbative crossover where the edge of the nonequilibrium distribution reaches Berry-curvature hot spots, a regime in which constant relaxation-time estimates and Berry curvature dipole calculations become unreliable. We further demonstrate that interaction and electron-phonon self-energies within dynamical mean-field theory can substantially change the Hall signal. Our framework enables quantitative simulations of nonequilibrium nonlinear Hall phenomena and provides guidance for strong-field transport experiments.

The interplay between topology, nonequilibrium and correlations is an outstanding challenge in quantum condensed matter physics. For example, electrical transport can reveal signatures of topology, although in correlated settings, theoretical studies are generally difficult. Consider the Hall effect, which is a central paradigm of condensed matter physics, linking transverse transport to the symmetry, topology, and geometry of electronic states. In the linear regime, a Hall current without an external magnetic field requires broken time-reversal symmetry, as in the anomalous Hall effect. This constraint is lifted beyond linear response: in time-reversal-invariant but inversion-breaking systems, a longitudinal electric field can drive a transverse current at second order, giving rise to the nonlinear Hall effect [1–3]. The simplest picture is the Berry curvature dipole—the electric field shifts the distribution of occupied states, producing a net anomalous velocity even though the Berry curvature integrates to zero in equilibrium [1, 4, 5]. This mechanism yields rectified and second-harmonic Hall responses, and it can be used to detect momentum-space Berry curvature in nonmagnetic materials.

The nonlinear Hall effect has rapidly evolved from a theoretical proposal into an experimental probe of quantum materials. Second-order Hall signals were observed in inversion-breaking, time-reversal-symmetric systems, including bilayer and few-layer  $\text{WTe}_2$  [6, 7], the ultrathin Weyl semimetal  $\text{TaIrTe}_4$  [8], and the 3D Weyl-Kondo semimetal  $\text{Ce}_3\text{Bi}_4\text{Pd}_3$  [9]. The observation of a giant nonlinear Hall response in  $\text{Ce}_3\text{Bi}_4\text{Pd}_3$  marked a key advance, providing compelling bulk transport evidence for the Weyl-Kondo semimetal state [10, 11]. Higher-order responses have further been analyzed in terms of Berry-curvature multipoles and related geometric quantities [12–14].

On the theoretical side, weak-field perturbative studies have been performed beyond the original Berry curvature

dipole picture [1]. Quantum kinetic and diagrammatic approaches have shown that disorder-induced side-jump and skew-scattering processes enter at the same order as the Berry-curvature-dipole contribution and can substantially modify the nonlinear Hall response [15–18]. Recent work has also clarified the connection between semiclassical Boltzmann theory and quantum perturbation theory, emphasizing the roles of dissipation and multiband geometry [19–22]. In parallel, relaxation-time-independent intrinsic mechanisms have been formulated in terms of the Berry-connection polarizability [23–25]. Such geometric mechanisms play an important role in magnetic systems [26–29].

While these developments reveal a rich interplay of Berry curvature, quantum metric, disorder, and dissipation in perturbative nonlinear Hall transport, the nonperturbative strong-field regime remains underexplored. First experimental evidence for this strong-field regime was found in  $\text{Ce}_3\text{Bi}_4\text{Pd}_3$ , where the Hall resistivity strongly deviates from Berry-curvature-dipole scaling [9]. Similar behavior was also found in Boltzmann-equation studies, when the driven distribution crosses Berry-curvature hot spots [30]. To systematically explore the nonperturbative regime, including the role of dissipation and electron correlations, we develop a steady-state framework for dc-field-driven lattice systems, based on nonequilibrium Green's functions (NEGF). While NEGF calculations have recently been applied to ultrafast nonlinear Hall dynamics [31], we focus on time-translationally invariant steady states under a constant electric field, following approaches developed for photodoped [32–36] and electric-field-driven [37–42] systems. In this framework, the uniform dc field is incorporated through the gauge-covariant Wigner representation, where the electric field enters via the Moyal star product [43, 44]. The natural momentum variable in this representation is the gauge-covariant momentum  $\kappa$ , which

reduces to the usual momentum in the absence of the field [45]. Dissipation is introduced through the coupling to external baths, which stabilizes a nonequilibrium steady state. In contrast to semiclassical Boltzmann-equation approaches, the NEGF formulation retains interband coherence, treats the driving field nonperturbatively, and incorporates interactions and electron-phonon coupling through frequency-dependent self-energies. It does not rely on a quasi-particle approximation and allows to compute the Hall current without relying on the Berry-curvature-dipole picture. The full details of the derivation of the formalism and the numerical implementation are provided in the Supplemental Material [46].

We apply this framework to a minimal two-band lattice model that contains the key ingredients for the nonlinear Hall effect in a time-reversal-invariant but inversion-broken system. The Hamiltonian is

$$H(\mathbf{k}) = (\cos k_x - D_x)\sigma_x + \sin k_y \sigma_y + (\cos k_y - D_y)\sigma_z, \quad (1)$$

where  $\sigma_{\alpha=x,y,z}$  are Pauli matrices in orbital space [47]. In the following, we use  $D_x = 0.5$  and  $D_y = 1.0$ , and set the lattice constant and hopping to unity. For these parameters, the model describes a semimetal with two Weyl-like points. The band dispersion is shown in Fig. 1(a), together with the Berry-curvature distribution plotted on the  $\varepsilon = 0$  plane. Because time-reversal symmetry is preserved, the Berry curvature is odd in momentum and integrates to zero over the Brillouin zone. It is strongly concentrated near the two Weyl-like points, where it has opposite signs.

We consider the response to a dc electric field applied along the  $x$  direction. In the semiclassical picture, the Berry curvature contributes to the transverse current through the anomalous velocity,  $\mathbf{v}_{\text{anom}} = -\mathbf{E} \times \boldsymbol{\Omega}_n(\mathbf{k})$ . Thus, the Hall response is obtained from a Berry-curvature-weighted occupation [48],

$$\frac{J_y}{E_x} = \sum_{\nu} \int_{\text{BZ}} \frac{d^2k}{(2\pi)^2} n_{\nu}(\mathbf{k}) \Omega_{\nu}^z(\mathbf{k}), \quad (2)$$

where  $n_{\nu}(\mathbf{k})$  and  $\Omega_{\nu}^z(\mathbf{k})$  are the occupation and Berry curvature of band  $\nu$ . In equilibrium this integral vanishes in time-reversal-invariant systems, but an electric field can distort the occupation and make it finite. In the weak-field limit, this becomes the Berry-curvature-dipole mechanism [1], which is directly implemented in Boltzmann-equation treatments [30, 48]. The NEGF formalism, by contrast, can evaluate the Hall current more generally using the velocity operator  $v_y(\boldsymbol{\kappa}) = \partial H(\boldsymbol{\kappa}) / \partial \kappa_y$ ,

$$J_y = \int_{\text{BZ}} \frac{d^2\kappa}{(2\pi)^2} \text{Tr}[v_y(\boldsymbol{\kappa}) \tilde{n}(\boldsymbol{\kappa})], \quad (3)$$

where  $\tilde{n}(\boldsymbol{\kappa}) = -i\tilde{G}^<(\tau = 0, \boldsymbol{\kappa}) = -iG^<(\tau = 0, \boldsymbol{\kappa} + q\mathbf{A})$  is the gauge-covariant equal-time density matrix in the field-driven steady state, with  $G^<$  the lesser Green's function and  $\mathbf{A}$  the vector potential. In the field-free band basis of the present model, the transverse current is carried by the interband-coherence component of  $\tilde{n}(\boldsymbol{\kappa})$ .

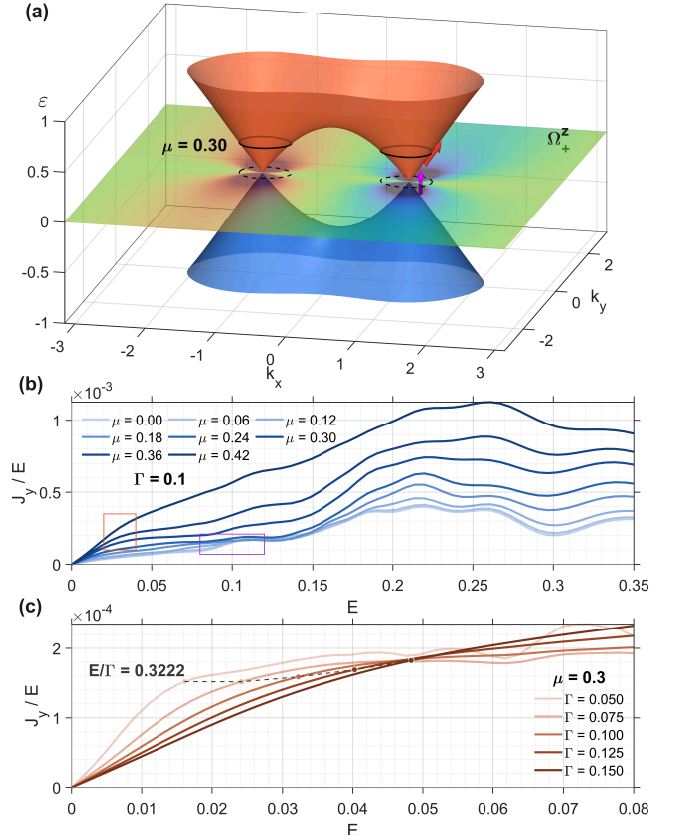


FIG. 1. (a) Band structure of the two-band model in the  $(k_x, k_y)$  plane, with the Berry curvature of the upper band projected onto the  $\varepsilon = 0$  plane and the Fermi contour for  $\mu = 0.30$  indicated. The red and magenta arrows denote representative intraband and interband electron transfer processes near the right cone under a constant electric field. (b) Field-normalized transverse current  $J_y/E$  as a function of the driving field  $E$  for several chemical potentials  $\mu$  at fixed scattering rate  $\Gamma = 0.1$ . (c)  $J_y/E$  as a function of  $E$  for several scattering rates  $\Gamma$  at fixed chemical potential  $\mu = 0.30$ . The dots connected by the dashed line indicate the condition  $E/\Gamma = \Delta k_x$ , where  $\Delta k_x = 0.3222$  is the distance between the Weyl-like point and the equilibrium Fermi surface.

In the weak-field perturbative regime, the electric field mainly distorts the occupation near the Fermi surface, and the NEGF result reduces to the Berry-curvature-dipole description. For Dirac or Weyl semimetals, however, this perturbative picture becomes incomplete when the field is strong or when the Fermi surface lies close to a nodal point [9, 30]. In this regime, field-induced interband charge transfer near the cones contributes to the current, as indicated by the magenta arrows in Fig. 1(a). This goes beyond the Berry-curvature-dipole description, and even the more general anomalous-velocity formula Eq. (2) is not guaranteed to reproduce the full Hall current due to the interband coherence [49]. The NEGF approach, on the other hand, remains applicable even in the semimetallic case  $\mu = 0$ , where no conventional Fermi surface is present.

To quantify the field and doping dependence, Fig. 1(b) shows  $J_y/E$  for several chemical potentials. The system is coupled to a zero-temperature fermionic bath with chemical potential  $\mu$  and constant retarded self-energy  $\Sigma_{\text{bath}}^R = -i\Gamma$ , with  $\Gamma = 0.1$ . At weak fields,  $J_y/E$  is approximately linear in  $E$ , corresponding to the perturbative scaling  $J_y \propto E^2$ . This behavior persists even at  $\mu = 0$ , where no conventional Fermi surface exists and the response is instead driven by field-induced interband charge transfer near the cones. As  $\mu$  is increased, the magnitude of the Hall response grows. For low and intermediate chemical potentials, the field dependence, especially at stronger fields, remains similar to the semimetallic case, indicating that interband processes still play an important role.

For larger chemical potentials, the curves bend near  $E \simeq 0.03$ , as highlighted by the orange box in Fig. 1(b). This marks the onset of the nonperturbative drift mechanism: the field-driven Fermi-contour edge reaches the Berry-curvature hot spot near a Weyl-like point [30]. Beyond this point, the weak-field Berry-curvature-dipole expansion is no longer controlled for the reasons discussed above, even if  $J_y/E$  remains approximately linear over some field range. At still stronger fields, especially when  $E$  becomes comparable to the damping scale  $\Gamma$ , additional deviations appear, including the bump structure marked by the purple box in Fig. 1(b). The response eventually enters a fully nonperturbative regime, where the Hall signal can even decrease with increasing field.

These observations show that the Berry-curvature-dipole picture is reliable only in the large- $\mu$ , weak-field region of Fig. 1(b), where the response is governed by a small intraband displacement of an existing Fermi surface and the Fermi-contour edge remains sufficiently far from the Weyl-point-like hot spots. Outside this region, either interband charge transfer or strong-field redistribution becomes important, and the full NEGF density-matrix treatment is needed.

We next examine the nonperturbative drift mechanism highlighted by the orange box. We fix  $\mu = 0.3$  and compute  $J_y/E$  for several damping rates  $\Gamma$ , as shown in Fig. 1(c). For this chemical potential, the Fermi-contour edge is separated from the nearest Weyl-like point by  $\Delta\kappa_x = 0.3222$ . Using the drift estimate  $\Delta\kappa_x \simeq E/\Gamma$ , the crossover is expected at  $E^* \simeq \Gamma\Delta\kappa_x$ . The corresponding values are marked in Fig. 1(c) and connected by a dashed line. Their agreement with the bending points of the Hall response supports the interpretation that the crossover is controlled by the field-driven shift of the Fermi contour to a Berry-curvature hot spot.

To visualize the momentum-space evolution associated with intra- and interband processes, we plot representative occupations  $\text{Tr} \tilde{n}(\boldsymbol{\kappa})$  in Fig. 2 for  $\Gamma = 0.1$ . We first consider the case with  $\mu = 0.3$ , where the nonperturbative crossover is driven by intraband drift. As shown in Fig. 2(a), at  $E^* \simeq \Gamma\Delta\kappa_x = 0.0322$ , the occupation edge is displaced to the vicinity of the Weyl-like point. This directly illustrates the drift mechanism responsible for the nonperturbative feature marked by the orange box in Fig. 1(b), in qualitative agreement with the picture proposed in Ref. [30].

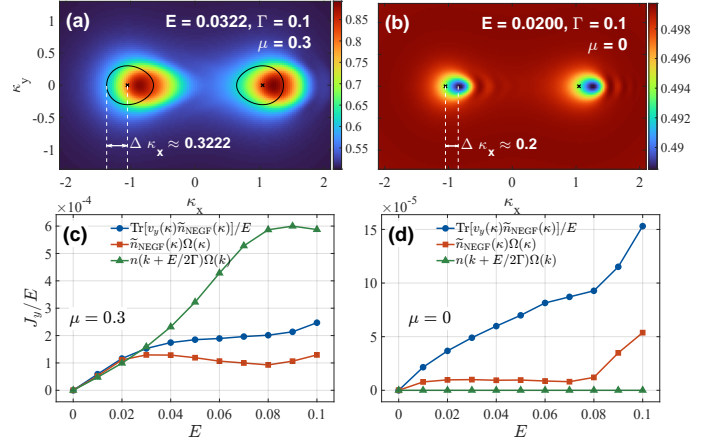


FIG. 2. (a,b) Momentum-resolved occupation  $\text{Tr} \tilde{n}(\boldsymbol{\kappa})$  for  $\mu = 0.3$  and  $\mu = 0$ , respectively, at the indicated value of  $E$ . Black crosses mark the Weyl-like points, and the black contour in (a) shows the Fermi surface. The dashed white lines indicate the characteristic momentum interval  $\Delta\kappa_x$ . (c,d) Hall-current response  $J_y/E$  as a function of the electric field  $E$  for  $\mu = 0.3$  and  $\mu = 0$ , comparing the NEGF result  $\text{Tr}[v_y(\boldsymbol{\kappa})\tilde{n}_{\text{NEGF}}(\boldsymbol{\kappa})]/E$ , the Berry-curvature estimate  $\tilde{n}_{\text{NEGF}}(\boldsymbol{\kappa})\Omega(\boldsymbol{\kappa})$ , and the shifted-equilibrium estimate  $n(\mathbf{k} + E/2\Gamma)\Omega(\mathbf{k})$ . All the calculations use  $\Gamma = 0.1$ .

We then turn to the semimetallic case  $\mu = 0$ , where the response is driven by field-induced interband charge transfer. Figure 2(b) shows two hole-like structures displaced from the corresponding Weyl-like points by approximately  $E/\Gamma$  along the field direction, accompanied by oscillatory tails [50]. Since vertical interband excitation at fixed momentum conserves  $\text{Tr} \tilde{n}(\boldsymbol{\kappa})$ , the observed hole-like structures reflect field- and dissipation-induced momentum-space redistribution, which can generate a Hall response in the anomalous-velocity picture through the opposite Berry curvatures of the two bands.

However, this does not imply that Eq. (2) is quantitatively reliable for the Hall response induced by interband processes. In the direct NEGF calculation, the Hall current is evaluated by Eq. (3). For comparison, we transform the density matrix to the field-free band basis and evaluate Eq. (2). The results for different  $\mu$  are shown in Figs. 2(c) and 2(d). In the weak-field regime and for nonzero chemical potential, the Berry-curvature-weighted estimate agrees well with the full NEGF current. Once interband processes become important, however, the discrepancy becomes pronounced. This is the case both for  $\mu = 0$ , where the response is intrinsically interband, and for the nonperturbative regime at  $\mu = 0.3$ , where the Fermi contour approaches the Weyl-like point and interband effects become significant. Thus, even when the same density matrix is used, Eq. (2) fails to reproduce the full Hall current when interband processes play a role. This comparison also highlights a limitation of the Boltzmann-equation method based on the Berry curvature dipole.

It is also interesting to compare our results with the perturbative constant relaxation-time or constant scattering-rate

calculations, which are in fact not equivalent. To see this, consider the weak-field distortion of the momentum distribution at zero temperature,

$$\tilde{n}(\boldsymbol{\kappa}) = \tilde{n}_0(\boldsymbol{\kappa}) - \Delta\kappa \partial_{\kappa_x} \tilde{n}_0(\boldsymbol{\kappa}). \quad (4)$$

In a constant relaxation-time approximation, the displacement is momentum independent,  $\Delta\kappa_{\tau_B} = E\tau_B$ , where  $\tau_B$  is the Boltzmann relaxation time. By contrast, in the constant scattering-rate approximation, the effective displacement depends on the distance from the chemical potential,  $\Delta\kappa_{\Gamma}(\boldsymbol{\kappa}) = E\Gamma/\{\mu - \epsilon(\boldsymbol{\kappa})\}^2 + \Gamma^2\}$  [46], which is largest near the Fermi surface,  $\Delta\kappa_{\Gamma} = E/\Gamma$ , and rapidly decreases away from it. For weak fields and small  $\Gamma$ , the two descriptions can be approximately matched by choosing  $\tau_B = 1/(2\Gamma)$ , corresponding to an average displacement  $\Delta\kappa_{\tau_B} = E/(2\Gamma)$ . At larger fields, however, the broadening effect leads to noticeable deviations from a simple rigid-shift picture. Using this identification, we compare in Figs. 2(c) and 2(d) the NEGF result with a Berry-curvature-dipole estimate obtained by rigidly shifting the equilibrium density matrix by  $E/(2\Gamma)$ . This construction captures only the intraband redistribution and therefore cannot describe the interband mechanism; consequently, it gives no Hall response in the semimetallic case  $\mu = 0$ . For  $\mu = 0.3$ , the shifted-distribution estimate agrees reasonably well with the NEGF result in the weak-field regime. However, it predicts a different position for the nonperturbative crossover. The reason is that the crossover is controlled by the actual displacement of states on the Fermi contour, which is  $E/\Gamma$  in the constant scattering-rate approximation used in the NEGF calculation, twice the value of the matched relaxation-time estimate. As a result, the Fermi-contour edge reaches the Weyl-like point at a smaller field. This comparison shows that the choice of dissipation model is not a minor detail: it can determine the field scale at which the nonperturbative crossover occurs.

So far, we have used a bath with a constant retarded self-energy. This assumption, however, is not required in the NEGF framework. Frequency-dependent bath self-energies, electron-phonon coupling, and interaction effects can be incorporated into the calculations, although the numerical solution becomes more demanding. The corresponding formulations are described in the Supplemental Material [46].

This more general implementation also gives access to frequency-resolved quantities. Figures 3(a) and 3(b) show the momentum-resolved spectral function and occupied spectral weight along a high-symmetry path for a Lorentzian fermionic bath with peak amplitude  $\Gamma = 0.1$  and half-width  $W = 4$ , at  $T = 1/30$ ,  $\mu = 0.3$ , and  $E = 0.09$ . The stripe-like structures along the  $\Gamma$ - $X$  path are a spectral signature of interband resonances. We note that the imaginary part of the momentum-resolved lesser Green's function in the Wigner representation should be interpreted as a quasi-distribution rather than a positive-definite probability density. It can therefore display negative values, while its frequency-integrated momentum distribution, shown in Fig. 2, and its momentum-

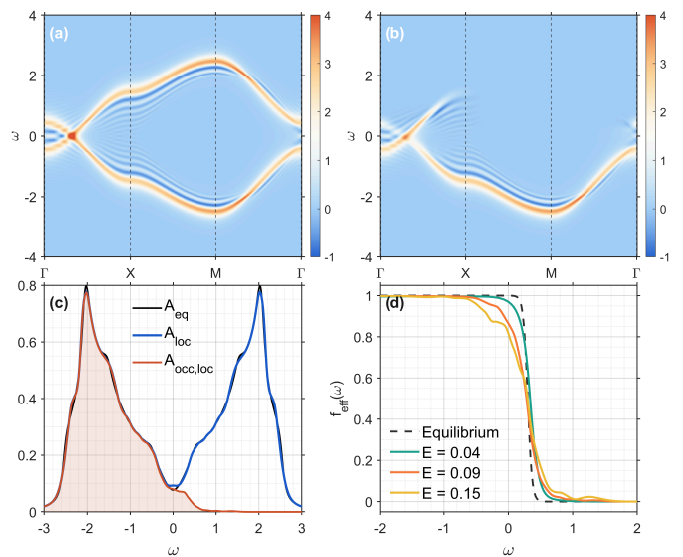


FIG. 3. (a) Spectral function  $\text{Tr} A(\omega, \kappa_{\text{path}})$  and (b) occupied spectral function  $\text{Tr} A_{\text{occ}}(\omega, \kappa_{\text{path}})$  along the high-symmetry path  $\Gamma$ - $X$ - $M$ - $\Gamma$ , together with (c) the full local spectrum  $A_{\text{loc}}(\omega)$  and occupied local spectrum  $A_{\text{occ,loc}}(\omega)$ , for the representative case  $E = 0.09$ . (d) Effective local distribution function  $f_{\text{eff}}(\omega)$  in equilibrium and under driving fields  $E = 0.04, 0.09$ , and  $0.15$ .

integrated occupied spectral weight, shown in Fig. 3(c), remain positive.

We further extract an effective distribution function  $f_{\text{eff}}(\omega) = \text{Tr} A_{\text{loc,occ}}(\omega)/\text{Tr} A_{\text{loc}}(\omega)$  from the local occupied spectral weight and the local spectral function in Fig. 3(c). The result is shown in Fig. 3(d). At weak field, for example  $E = 0.04$ , the distribution already deviates from the equilibrium Fermi function but remains smooth. At stronger fields, pronounced wiggles and a clear left-right asymmetry appear. The detailed form of these structures depends on the band dispersion, but their emergence signals the breakdown of the perturbative regime and the formation of a strongly driven nonequilibrium steady state.

We are now in position to address the interaction effects to the Hall response. Starting from the Lorentzian fermionic bath setup discussed above, we include either an electron-phonon coupling to a phonon mode with  $\omega_0 = 1$  or a local Hubbard interaction with  $U = 0.8$  within dynamical mean-field theory (DMFT) [51]. The phonons are treated in the Migdal approximation, and the interactions using boldfied second-order perturbation theory. The resulting Hall responses are compared with the bath-only result in Fig. 4(a). In all three cases, the overall field dependence remains similar, indicating that the nonperturbative mechanisms identified above are robust. We have also checked the corresponding longitudinal conductivity  $J_x/E$  and found that it is only weakly affected by the additional phonon coupling or local interaction in the parameter regime considered here. However, both the electron-phonon and interaction self-energies significantly enhance the magnitude of  $J_y/E$ .

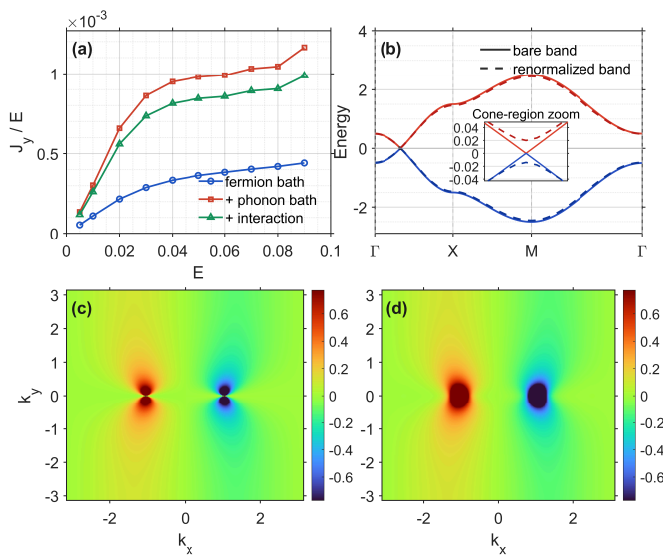


FIG. 4. (a) Field-normalized transverse current  $J_y/E$  as a function of the driving field  $E$  for three cases: coupling only to a fermionic bath, coupling to both fermionic and phononic baths, and the interacting case. (b) Bare and phonon-renormalized band dispersions along the high-symmetry path  $\Gamma$ - $X$ - $M$ - $\Gamma$ , with an inset showing a magnified view of the Weyl-like region to highlight the gap opened by the real part of the self-energy  $\Sigma_{\text{ph}}$ . (c) Bare and (d) phonon-renormalized Berry curvature of the upper band across the Brillouin zone.

At first sight, this enhancement may appear counterintuitive. Additional interactions or phonon scattering are expected to increase the imaginary part of the self-energy and thus suppress the Hall response. In the present parameter regime, however, the dominant effect comes from the real part of the self-energy, which renormalizes the band structure and the associated Berry curvature. To illustrate this point, we extract the quasiparticle dispersion from the equilibrium electron-phonon self-energy by solving the equation

$$\det[\omega + \mu - H(\mathbf{k}) - \text{Re} \Sigma_{\text{ph}}^R(\omega)] = 0. \quad (5)$$

The resulting effective bands are shown in Fig. 4(b). The electron-phonon coupling slightly flattens the bands and, more importantly, opens a small gap near the Weyl-like point.

Although the changes in the correlated bandstructure are modest on the scale of the full bandwidth, they have a strong effect on the nonlinear Hall response. The Berry curvature is concentrated near the Weyl-like point, and therefore even a small gap opening or band deformation in this region can substantially modify the Berry-curvature hot spots. Figures 4(c) and 4(d) compare the Berry curvature of the bare band structure with that computed from the phonon-renormalized quasiparticle bands. The renormalized bands exhibit stronger Berry-curvature hot spots, which explains the enhanced Hall response in Fig. 4(a). To demonstrate the dominant role of the gap opening, we also simulated model (1) with the parameter  $D_y$  modified as  $D_y^{\text{eff}} = D_y - \text{Re} \Sigma_z^R(\omega = 0)$ , with  $\Sigma_z$  the

antisymmetric component of the self-energy in orbital space [46]. For fields  $E \lesssim 0.1$ , this calculation reproduces the Hall current of the full many-body calculation within a few percent.

In summary, we studied the Berry-curvature-induced nonlinear Hall transport in the nonperturbative regime and in the presence of electron correlations by employing a nonequilibrium steady-state Green's function approach for dc-field-driven lattice systems. The method treats the electric field nonperturbatively and gives access to the momentum- and frequency-resolved nonequilibrium electronic structure. For a two-band model, we showed that the Berry-curvature-dipole picture is controlled only at sufficiently large doping and weak fields. It breaks down when the driven Fermi-contour edge reaches the Weyl-point-like Berry-curvature hot spots, or when interband charge transfer becomes important in the semimetallic regime. We also clarified that constant relaxation-time and constant scattering-rate descriptions can predict different crossover fields. In the nonperturbative regimes, Berry-curvature-weighted occupation formulas no longer reliably reproduce the full Hall current, which is instead obtained directly within the NEGF framework. The formalism also makes it possible to incorporate dissipation, interactions, and electron-phonon coupling through self-energies, going beyond the constant relaxation-time approximation. Our DMFT calculations showed that interactions and electron-phonon coupling can substantially change the Hall response, not only through additional damping but also through band renormalizations and gap openings, and the resulting modifications of Berry-curvature hot spots. These results demonstrate a flexible numerical framework for nonperturbative nonequilibrium nonlinear Hall phenomena and offer guidance for strong-field transport and spectroscopic experiments.

*Acknowledgments* The calculations were run on the Beo06 cluster at the University of Fribourg. This work was supported by the Swiss National Science Foundation via NCCR Marvel and Grant No. 2000-1-240023, by the German Research Foundation through research unit QUAST (FOR 5249), and the Austrian Science Fund via Grant 10.55776/I5868 (QUAST). Work at Rice University has been supported by the National Science Foundation under Grant No. DMR-2220603 (L.C., S.S. and Q.S.), and by the Robert A. Welch Foundation Grant No. C-1411 (Q.S.) and the Vannevar Bush Faculty Fellowship ONR-VB N00014-23-1-2870 (Q.S.). M. E. acknowledges discussions with Karsten Held. L.C., S. P., Q.S. and P. W. acknowledge the hospitality of the Aspen Center for Physics, which is supported by the National Science Foundation under Grant No. PHY-2210452 and a grant from the Simons Foundation (1161654, Troyer).

\* lei.geng@unifr.ch

† philipp.werner@unifr.ch

[1] I. Sodemann and L. Fu, Quantum nonlinear hall effect induced

- by berry curvature dipole in time-reversal invariant materials, *Phys. Rev. Lett.* **115**, 216806 (2015).
- [2] Z. Du, H.-Z. Lu, and X. Xie, Nonlinear hall effects, *Nat. Rev. Phys.* **3**, 744 (2021).
- [3] A. Bandyopadhyay, N. B. Joseph, and A. Narayan, Non-linear hall effects: Mechanisms and materials, *Mater. Today Electron.* **8**, 100101 (2024).
- [4] E. Deyo, L. Golub, E. Ivchenko, and B. Spivak, Semi-classical theory of the photogalvanic effect in non-centrosymmetric systems, arXiv preprint arXiv:0904.1917 10.48550/arXiv.0904.1917 (2009).
- [5] J. E. Moore and J. Orenstein, Confinement-induced berry phase and helicity-dependent photocurrents, *Phys. Rev. Lett.* **105**, 026805 (2010).
- [6] Q. Ma, S.-Y. Xu, H. Shen, D. MacNeill, V. Fatemi, A. M. Mier Valdivia, S. Wu, T.-R. Chang, Z. Du, C.-H. Hsu, Q. D. Gibson, S. Fang, E. Kaxiras, K. Watanabe, T. Taniguchi, R. J. Cava, H.-Z. Lu, H. Lin, L. Fu, N. Gedik, and P. Jarillo-Herrero, Observation of the nonlinear hall effect under time-reversal-symmetric conditions, *Nature* **565**, 337 (2019).
- [7] K. Kang, T. Li, E. Sohn, J. Shan, and K. F. Mak, Nonlinear anomalous hall effect in few-layer  $\text{WTe}_2$ , *Nat. Mater.* **18**, 324 (2019).
- [8] D. Kumar, C.-H. Hsu, R. Sharma, T.-R. Chang, P. Yu, J. Wang, G. Eda, G. Liang, and H. Yang, Room-temperature nonlinear hall effect and wireless radiofrequency rectification in weyl semimetal  $\text{TaIrTe}_4$ , *Nat. Nanotechnol.* **16**, 421 (2021).
- [9] S. Dzsaber, X. Yan, M. Taupin, G. Eguchi, A. Prokofiev, T. Shiroka, P. Blaha, O. Rubel, S. E. Grefe, H.-H. Lai, *et al.*, Giant spontaneous hall effect in a nonmagnetic weyl-kondo semimetal, *Proc. Natl. Acad. Sci.* **118**, e2013386118 (2021).
- [10] H.-H. Lai, S. E. Grefe, S. Paschen, and Q. Si, Weyl-kondo semimetal in heavy-fermion systems, *Proc. Natl. Acad. Sci. U.S.A.* **115**, 93 (2018).
- [11] S. Dzsaber, L. Prochaska, A. Sidorenko, G. Eguchi, R. Svagera, M. Waas, A. Prokofiev, Q. Si, and S. Paschen, Kondo insulator to semimetal transformation tuned by spin-orbit coupling, *Phys. Rev. Lett.* **118**, 246601 (2017).
- [12] C.-P. Zhang, X.-J. Gao, Y.-M. Xie, H. C. Po, and K. T. Law, Higher-order nonlinear anomalous hall effects induced by berry curvature multipoles, *Phys. Rev. B* **107**, 115142 (2023).
- [13] C. Wang, R.-C. Xiao, H. Liu, Z. Zhang, S. Lai, C. Zhu, H. Cai, N. Wang, S. Chen, Y. Deng, Z. Liu, S. A. Yang, and W.-B. Gao, Room-temperature third-order nonlinear hall effect in weyl semimetal  $\text{TaIrTe}_4$ , *Natl. Sci. Rev.* **9**, nwac020 (2022).
- [14] S. Lai, H. Liu, Z. Zhang, J. Zhao, X. Feng, N. Wang, C. Tang, Y. Liu, K. Xu, W. Duan, and W.-B. Gao, Third-order nonlinear hall effect induced by the berry-connection polarizability tensor, *Nat. Nanotechnol.* **16**, 869 (2021).
- [15] Z. Z. Du, C. M. Wang, S. Li, H.-Z. Lu, and X. C. Xie, Disorder-induced nonlinear hall effect with time-reversal symmetry, *Nat. Commun.* **10**, 3047 (2019).
- [16] S. Nandy and I. Sodemann, Symmetry and quantum kinetics of the nonlinear hall effect, *Phys. Rev. B* **100**, 195117 (2019).
- [17] C. Xiao, Z. Z. Du, and Q. Niu, Theory of nonlinear hall effects: Modified semiclassics from quantum kinetics, *Phys. Rev. B* **100**, 165422 (2019).
- [18] Z. Z. Du, C. M. Wang, H.-P. Sun, H.-Z. Lu, and X. C. Xie, Quantum theory of the nonlinear hall effect, *Nat. Commun.* **12**, 5038 (2021).
- [19] D. Kaplan, T. Holder, and B. Yan, Unifying semiclassics and quantum perturbation theory at nonlinear order, *SciPost Phys.* **14**, 082 (2023).
- [20] Y. Michishita and N. Nagaosa, Dissipation and geometry in nonlinear quantum transports of multiband electronic systems, *Phys. Rev. B* **106**, 125114 (2022).
- [21] Y. Tokura and N. Nagaosa, Nonreciprocal responses from non-centrosymmetric quantum materials, *Nat. Commun.* **9**, 3740 (2018).
- [22] Y. Fang, S. Sur, Y. Xie, and Q. Si, Nonlinear thermal and thermoelectric transport from quantum geometry, arXiv preprint arXiv:2505.16999 <https://doi.org/10.48550/arXiv.2505.16999> (2025).
- [23] Y. Gao, S. A. Yang, and Q. Niu, Field induced positional shift of bloch electrons and its dynamical implications, *Phys. Rev. Lett.* **112**, 166601 (2014).
- [24] C. Wang, Y. Gao, and D. Xiao, Intrinsic nonlinear hall effect in antiferromagnetic tetragonal  $\text{CuMnAs}$ , *Phys. Rev. Lett.* **127**, 277201 (2021).
- [25] H. Liu, J. Zhao, Y.-X. Huang, W. Wu, X.-L. Sheng, C. Xiao, and S. A. Yang, Intrinsic second-order anomalous hall effect and its application in compensated antiferromagnets, *Phys. Rev. Lett.* **127**, 277202 (2021).
- [26] D. Kaplan, T. Holder, and B. Yan, General nonlinear hall current in magnetic insulators beyond the quantum anomalous hall effect, *Nat. Commun.* **14**, 3053 (2023).
- [27] D. Kaplan, T. Holder, and B. Yan, Unification of nonlinear anomalous hall effect and nonreciprocal magnetoresistance in metals by the quantum geometry, *Phys. Rev. Lett.* **132**, 026301 (2024).
- [28] A. Gao, Y.-F. Liu, J.-X. Qiu, B. Ghosh, T. V. Trevisan, Y. Onishi, C. Hu, T. Qian, H.-J. Tien, S.-W. Chen, M. Huang, D. Bérubé, H. Li, C. Tzschaschel, T. Dinh, Z. Sun, S.-C. Ho, S.-W. Lien, B. Singh, K. Watanabe, T. Taniguchi, D. C. Bell, H. Lin, T.-R. Chang, C. R. Du, A. Bansil, L. Fu, N. Ni, P. P. Orth, Q. Ma, and S.-Y. Xu, Quantum metric nonlinear hall effect in a topological antiferromagnetic heterostructure, *Science* **381**, 181 (2023).
- [29] N. Wang, D. Kaplan, Z. Zhang, T. Holder, N. Cao, A. Wang, X. Zhou, F. Zhou, Z. Jiang, C. Zhang, S. Ru, H. Cai, K. Watanabe, T. Taniguchi, B. Yan, and W. Gao, Quantum-metric-induced nonlinear transport in a topological antiferromagnet, *Nature* **621**, 487 (2023).
- [30] S. Sur, L. Chen, Y. Wang, C. Setty, S. Paschen, and Q. Si, Fully nonequilibrium hall response from berry curvature, arXiv preprint arXiv:2411.16675 (2024).
- [31] M. Dendzik, A. Marini, S. Beaulieu, S. Dong, T. Pincelli, J. Maklar, R. P. Xian, E. Perfetto, M. Wolf, G. Stefanucci, *et al.*, Ultrafast nonlinear hall effect in black phosphorus, arXiv preprint arXiv:2604.06083 (2026).
- [32] J. Li and M. Eckstein, Nonequilibrium steady-state theory of photodoped mott insulators, *Phys. Rev. B* **103**, 045133 (2021).
- [33] Y. Murakami, D. Golež, M. Eckstein, and P. Werner, Photoinduced nonequilibrium states in mott insulators, *Rev. Mod. Phys.* **97**, 035001 (2025).
- [34] L. Geng, A. J. Kim, and P. Werner, High-temperature  $\eta$ -pairing superconductivity in the photodoped hubbard model, arXiv preprint arXiv:2602.17238 (2026).
- [35] L. Geng, S. Ray, and P. Werner, Photoinduced excitonic magnetism in a multiorbital hubbard system, *Phys. Rev. B* **113**, 035143 (2026).
- [36] L. Geng, A. J. Kim, and P. Werner, Third-order strong-coupling impurity solver for real-frequency dynamical mean field theory: Accurate spectral functions for antiferromagnetic and photodoped states, *Phys. Rev. B* **112**, 245119 (2025).
- [37] Y. Murakami and P. Werner, Nonequilibrium steady states of electric field driven mott insulators, *Phys. Rev. B* **98**, 075102 (2018).

- [38] J. Li, C. Aron, G. Kotliar, and J. E. Han, Electric-field-driven resistive switching in the dissipative hubbard model, *Phys. Rev. Lett.* **114**, 226403 (2015).
- [39] J. E. Han, J. Li, C. Aron, and G. Kotliar, Nonequilibrium mean-field theory of resistive phase transitions, *Phys. Rev. B* **98**, 035145 (2018).
- [40] C. Aron, G. Kotliar, and C. Weber, Dimensional crossover driven by an electric field, *Phys. Rev. Lett.* **108**, 086401 (2012).
- [41] C. Aron, Dielectric breakdown of a mott insulator, *Phys. Rev. B* **86**, 085127 (2012).
- [42] C. Aron, C. Weber, and G. Kotliar, Impurity model for non-equilibrium steady states, *Phys. Rev. B* **87**, 125113 (2013).
- [43] H. J. Groenewold, On the principles of elementary quantum mechanics, in *On the principles of elementary quantum mechanics* (Springer, 1946) pp. 1–56.
- [44] J. E. Moyal, Quantum mechanics as a statistical theory, in *Mathematical Proceedings of the Cambridge Philosophical Society*, Vol. 45 (Cambridge University Press, 1949) pp. 99–124.
- [45] More precisely, the Green’s function written as a function of  $\kappa$  is the gauge-covariant Wigner Green’s function  $\tilde{G}(X, \kappa) = G(X, \kappa + q\mathbf{A}(X))$ , where  $\mathbf{A}(X)$  is the vector potential. Thus formulas written in terms of the ordinary momentum argument can be used in the gauge-covariant representation by evaluating them at  $\kappa$ .
- [46] See supplemental material at [url will be inserted by publisher] for the derivation of the gauge-covariant steady-state green’s-function formalism, details of the numerical implementation, and additional results.
- [47] In a minimal linearized  $k \cdot p$  model of a single cone, a tilt term proportional to  $\sigma_0$  is needed to reproduce the asymmetric nonequilibrium distribution near the cone. In Eq. (1), this effect arises from the full lattice momentum dependence, and no explicit  $\sigma_0$  term is required.
- [48] M. Gradhand, D. Fedorov, F. Pientka, P. Zahn, I. Mertig, and B. Györfy, First-principle calculations of the berry curvature of bloch states for charge and spin transport of electrons, *Journal of Physics: Condensed Matter* **24**, 213202 (2012).
- [49] D. Culcer, A. Sekine, and A. H. MacDonald, Interband coherence response to electric fields in crystals: Berry-phase contributions and disorder effects, *Phys. Rev. B* **96**, 035106 (2017).
- [50] The slight downward shift of the average occupation from 0.5 originates from finite time- and momentum-grid discretization errors. This nearly uniform offset does not affect the Hall current, which is computed directly from the converged density matrix.
- [51] H. Aoki, N. Tsuji, M. Eckstein, M. Kollar, T. Oka, and P. Werner, Nonequilibrium dynamical mean-field theory and its applications, *Rev. Mod. Phys.* **86**, 779 (2014).
- [52] S. Onoda, N. Sugimoto, and N. Nagaosa, Theory of nonequilibrium states driven by constant electromagnetic fields: —non-commutative quantum mechanics in the keldysh formalism—, *Progress of theoretical physics* **116**, 61 (2006).
- [53] J. K. Freericks and V. M. Turkowski, Steady-state nonequilibrium dynamical mean-field theory and the quantum boltzmann equation, *J. Phys.: Conf. Ser.* **35**, 39 (2006).
- [54] R. Bertoni and A. P. Jauho, Gauge-invariant formulation of the intracollisional field effect including collisional broadening, *Phys. Rev. B* **44**, 3655 (1991).
- [55] J. E. Han, Solution of electric-field-driven tight-binding lattice coupled to fermion reservoirs, *Phys. Rev. B* **87**, 085119 (2013).
- [56] Z. Dai, M. Manjappa, Y. Yang, T. C. W. Tan, B. Qiang, S. Han, L. J. Wong, F. Xiu, W. Liu, and R. Singh, High mobility 3d dirac semimetal ( $\text{Cd}_3\text{As}_2$ ) for ultrafast photoactive terahertz photonics, *Advanced Functional Materials* **31**, 2011011 (2021).
- [57] M. Neupane, S.-Y. Xu, R. Sankar, N. Alidoust, G. Bian, C. Liu, I. Belopolski, T.-R. Chang, H.-T. Jeng, H. Lin, *et al.*, Observation of a three-dimensional topological dirac semimetal phase in high-mobility  $\text{cd}_3\text{as}_2$ , *Nature communications* **5**, 3786 (2014).
- [58] A. Mosca Conte, O. Pulci, and F. Bechstedt, Electronic and optical properties of topological semimetal  $\text{cd}_3\text{as}_2$ , *Scientific Reports* **7**, 45500 (2017).
- [59] J. P. Carbotte, E. J. Nicol, and S. G. Sharapov, Effect of electron-phonon interaction on spectroscopies in graphene, *Phys. Rev. B* **81**, 045419 (2010).
- [60] B. Dóra and R. Moessner, Nonlinear electric transport in graphene: Quantum quench dynamics and the schwinger mechanism, *Phys. Rev. B* **81**, 165431 (2010).
- [61] D. Allor, T. D. Cohen, and D. A. McGady, Schwinger mechanism and graphene, *Phys. Rev. D* **78**, 096009 (2008).

## Supplemental Material for “Nonperturbative Nonlinear Hall Effect in Nonequilibrium Steady States”

### STEADY-STATE FORMALISM BASED ON NONEQUILIBRIUM GREEN’S FUNCTIONS

#### *Moyal product*

The nonlinear Hall effect under a constant electric field, and in the presence of dissipation, is a nonequilibrium phenomenon, which can be studied using nonequilibrium Green’s functions. In related previous works, the Green’s functions of nonequilibrium steady states were obtained by solving the Schwinger-Dyson equations self-consistently. Specifically, the retarded and lesser Green’s functions are obtained from [32, 37]

$$D * G^R = 1, \quad D \equiv (G_0^R)^{-1} - \Sigma^R, \quad (\text{S1})$$

and

$$G^< = G^R * \Sigma^< * G^A, \quad (\text{S2})$$

where  $*$  denotes the ordinary convolution. For a homogeneous steady state, the spatial dependence can be diagonalized in momentum space, so that the remaining convolution is only in time.

To reformulate the steady-state equations in a form suitable for systems with a constant electric field, it is useful to adopt the Wigner representation. As a simple example, consider the convolution of two two-time functions,

$$C(t_1, t_2) = \int dt_3 A(t_1, t_3) B(t_3, t_2). \quad (\text{S3})$$

We introduce the center-of-mass time and relative time,

$$T = \frac{t_1 + t_2}{2}, \quad t = t_1 - t_2, \quad (\text{S4})$$

and define the Wigner transform of a two-time function by

$$A(T, \omega) = \int dt e^{i\omega t} A\left(T + \frac{t}{2}, T - \frac{t}{2}\right). \quad (\text{S5})$$

In this representation, the convolution in Eq. (S3) is mapped to the Moyal, or star, product, denoted as  $\star$  [43, 44],

$$\begin{aligned} C(T, \omega) &= (A \star B)(T, \omega) \\ &= A(T, \omega) \exp \left[ \frac{i}{2} \left( \overleftarrow{\partial}_\omega \overrightarrow{\partial}_T - \overleftarrow{\partial}_T \overrightarrow{\partial}_\omega \right) \right] B(T, \omega). \end{aligned} \quad (\text{S6})$$

Left (right) arrows above the derivative operators indicate that they act on the left (right). Thus, even in the absence of external fields, the Wigner representation converts the original time convolution into a differential product structure in the  $(T, \omega)$  representation.

#### Gauge-covariant formulation

This formulation becomes especially useful when extending the theory to a system driven by a constant electric field [40]. In that case, it is no longer sufficient to work only with the time variables, because the electric field couples temporal and spatial degrees of freedom through the electromagnetic four-potential. It is therefore natural to generalize the Wigner representation from the two-time form discussed above to the full four-dimensional phase-space representation.

For functions depending on the center-of-mass coordinate  $X^\mu$  and conjugate four-momentum  $k^\mu$ , the ordinary Moyal product takes the form

$$A(X, k) \exp \left[ \frac{i}{2} \left( \overleftarrow{\partial}_{k^\mu} \overrightarrow{\partial}_{X_\mu} - \overleftarrow{\partial}_{X^\mu} \overrightarrow{\partial}_{k_\mu} \right) \right] B(X, k). \quad (\text{S7})$$

In the presence of an electromagnetic field, however, the Wigner representation must be reformulated in a gauge-covariant manner. This construction is standard in the derivation of quantum kinetic theory, where the usual Wigner transform is replaced by its gauge-invariant counterpart, equivalently expressed in terms of the kinetic momentum. To this end, one introduces the gauge-covariant four-momentum

$$\kappa^\mu = k^\mu - qA^\mu(X), \quad (\text{S8})$$

with  $A^\mu(X)$  the electromagnetic four-potential, and the Wigner Green's function  $\tilde{G}(X, \kappa) = G(X, \kappa + q\mathbf{A})$ . The Schwinger-Dyson equations then take the form of gauge-covariant Moyal star products in the  $(X, \kappa)$  variables [40, 52–54].

$$\begin{aligned} (A \star B)(X, \omega, \kappa) &= A(X, \omega, \kappa) \exp \left[ \frac{i}{2} \left( \overleftarrow{\partial}_{\kappa^\mu} \overrightarrow{\partial}_{X_\mu} - \overleftarrow{\partial}_{X^\mu} \overrightarrow{\partial}_{\kappa_\mu} \right) \right. \\ &\quad \left. + \frac{i}{2} q\mathbf{E} \cdot \left( \overleftarrow{\partial}_\omega \overrightarrow{\nabla}_\kappa - \overleftarrow{\nabla}_\kappa \overrightarrow{\partial}_\omega \right) \right] B(X, \omega, \kappa), \end{aligned} \quad (\text{S9})$$

where we have used  $\kappa^0 = \omega$  and  $\kappa = (\kappa^1, \kappa^2, \kappa^3)$ . The second term in the exponent is the field-induced contribution,

which mixes frequency and momentum derivatives and reflects the gauge-covariant structure of the steady-state problem under a dc field.

For a spatially uniform nonequilibrium steady state driven by a constant electric field, all quantities are independent of the center-of-mass time and space  $X$ , and the first term in the exponent of Eq. (S9) drops out. The star product then reduces to

$$\begin{aligned} (A \star B)(\omega, \kappa) &= \\ A(\omega, \kappa) \exp \left[ \frac{i}{2} q\mathbf{E} \cdot \left( \overleftarrow{\partial}_\omega \overrightarrow{\nabla}_\kappa - \overleftarrow{\nabla}_\kappa \overrightarrow{\partial}_\omega \right) \right] B(\omega, \kappa), \end{aligned} \quad (\text{S10})$$

and Schwinger-Dyson equations in a constant electric field are written in terms of this gauge-covariant star product rather than the ordinary convolution.

The gauge-covariant star product in Eq. (S10) can be implemented either in the frequency domain or in the time domain. For sufficiently strong electric fields, the frequency-domain formulation is advantageous, and has been used in earlier works [40–42]. In contrast, for weaker electric fields the time-domain formulation is generally more convenient from the numerical point of view. In the present study of the nonlinear Hall effect, we have examined both formulations. For the typical field strengths considered here, the time-domain approach exhibits faster convergence. We therefore focus in the following on the time-domain implementation of the star product and the associated Schwinger-Dyson equations.

For the time-domain solution of the Dyson equations with the gauge-covariant star product, we employ two different implementations. In one case, the self-energy is fully frequency dependent, while in the other it is approximated by a constant damping term. The latter case leads to substantial simplifications and can be solved much more efficiently numerically. In practice, a typical calculation within this simplified scheme requires only a few seconds on a 128-core computing node, whereas the frequency-dependent case may require several hours. We first describe the constant-damping approximation.

#### Constant self-energy

We start from Eq. (S1), with the ordinary convolution replaced by the gauge-covariant star product. Assuming that the retarded self-energy is approximated by a constant scattering term,  $\Sigma^R = -i\Gamma$ , we obtain

$$\left( \omega + i\Gamma - \epsilon(\kappa) \right) \star \tilde{G}^R(\omega, \kappa) = 1, \quad (\text{S11})$$

where  $\epsilon(\kappa)$  is the bare band dispersion.

Applying Eq. (S10) to Eq. (S11), one finds

$$\left[ \omega + i\Gamma + \frac{i}{2} \mathbf{E} \cdot \nabla_\kappa - \epsilon \left( \kappa - \frac{i}{2} \mathbf{E} \partial_\omega \right) \right] \tilde{G}^R(\omega, \kappa) = 1, \quad (\text{S12})$$

where we have absorbed the charge  $q$  into the definition of  $\mathbf{E}$  for notational simplicity.

We next perform a Fourier transform with respect to  $\omega$ , using

$$\omega \tilde{G}(\omega, \boldsymbol{\kappa}) \longleftrightarrow i\partial_\tau \tilde{G}(\tau, \boldsymbol{\kappa}), \quad \partial_\omega \tilde{G}(\omega, \boldsymbol{\kappa}) \longleftrightarrow i\tau \tilde{G}(\tau, \boldsymbol{\kappa}). \quad (\text{S13})$$

Equation (S12) is then transformed into

$$\left[ i\partial_\tau + i\Gamma + \frac{i}{2} \mathbf{E} \cdot \nabla_{\boldsymbol{\kappa}} - \epsilon \left( \boldsymbol{\kappa} + \frac{1}{2} \mathbf{E}\tau \right) \right] \tilde{G}^R(\tau, \boldsymbol{\kappa}) = \delta(\tau). \quad (\text{S14})$$

To eliminate the drift term, we introduce the comoving momentum variable

$$\boldsymbol{\kappa}' \equiv \boldsymbol{\kappa} - \frac{1}{2} \mathbf{E}\tau. \quad (\text{S15})$$

By the chain rule,

$$\partial_\tau \Big|_{\boldsymbol{\kappa}} = \partial_\tau \Big|_{\boldsymbol{\kappa}'} - \frac{1}{2} \mathbf{E} \cdot \nabla_{\boldsymbol{\kappa}'}, \quad \nabla_{\boldsymbol{\kappa}} \Big|_{\tau} = \nabla_{\boldsymbol{\kappa}'}, \quad (\text{S16})$$

so that

$$i\partial_\tau \Big|_{\boldsymbol{\kappa}} + \frac{i}{2} \mathbf{E} \cdot \nabla_{\boldsymbol{\kappa}} = i\partial_\tau \Big|_{\boldsymbol{\kappa}'}. \quad (\text{S17})$$

Defining  $G'^R(\tau, \boldsymbol{\kappa}') \equiv \tilde{G}^R(\tau, \boldsymbol{\kappa})$ , Eq. (S14) reduces to

$$[i\partial_\tau + i\Gamma - \epsilon(\boldsymbol{\kappa}' + \mathbf{E}\tau)] G'^R(\tau, \boldsymbol{\kappa}') = \delta(\tau). \quad (\text{S18})$$

Since  $G'^R$  is a retarded Green's function, it satisfies

$$G'^R(\tau, \boldsymbol{\kappa}') = 0, \quad \tau < 0, \quad (\text{S19})$$

and the discontinuity at  $\tau = 0$  implies

$$G'^R(0^+, \boldsymbol{\kappa}') = -i. \quad (\text{S20})$$

For  $\tau > 0$ , Eq. (S18) becomes a homogeneous first-order differential equation,

$$[i\partial_\tau + i\Gamma - \epsilon(\boldsymbol{\kappa}' + \mathbf{E}\tau)] G'^R(\tau, \boldsymbol{\kappa}') = 0, \quad (\text{S21})$$

whose solution is

$$G'^R(\tau, \boldsymbol{\kappa}') = -i\theta(\tau) \exp \left[ -\Gamma\tau - i \int_0^\tau d\tau' \epsilon(\boldsymbol{\kappa}' + \mathbf{E}\tau') \right]. \quad (\text{S22})$$

Transforming back to the original variable  $\boldsymbol{\kappa}$ , one obtains

$$\tilde{G}^R(\tau, \boldsymbol{\kappa}) = -i\theta(\tau) \exp \left[ -\Gamma\tau - i \int_{-\tau/2}^{\tau/2} d\tau' \epsilon(\boldsymbol{\kappa} + \mathbf{E}\tau') \right]. \quad (\text{S23})$$

This is the general expression for the retarded Green's function in the constant-damping approximation within the time-domain formulation under a uniform dc electric field.

We next consider the calculation of the lesser Green's function in Eq. (S2), with the ordinary convolution replaced by the star product. Using the Fourier transform together with

Eq. (S13), the dc star product in Eq. (S10) can be rewritten in the time domain as

$$(A \star B)(\tau, \boldsymbol{\kappa}) = \int d\tau_1 A \left( \tau_1, \boldsymbol{\kappa} + \frac{\mathbf{E}}{2}(\tau - \tau_1) \right) \times B \left( \tau - \tau_1, \boldsymbol{\kappa} - \frac{\mathbf{E}}{2}\tau_1 \right). \quad (\text{S24})$$

Since the bath self-energy  $\Sigma$  is independent of  $\boldsymbol{\kappa}$ , the star product of the first two factors in Eq. (S2) becomes

$$(\tilde{G}^R \star \Sigma^<)(\tau, \boldsymbol{\kappa}) = \int d\tau_1 \tilde{G}^R \left( \tau_1, \boldsymbol{\kappa} + \frac{\mathbf{E}}{2}(\tau - \tau_1) \right) \times \Sigma^<(\tau - \tau_1). \quad (\text{S25})$$

Applying the star product once more then yields

$$(\tilde{G}^R \star \Sigma^< \star \tilde{G}^A)(\tau, \boldsymbol{\kappa}) = \int d\tau_1 d\tau_2 \tilde{G}^R \left( \tau_1, \boldsymbol{\kappa} + \frac{\mathbf{E}}{2}(\tau - \tau_1) \right) \times \Sigma^<(\tau_2 - \tau_1) \tilde{G}^A \left( \tau - \tau_2, \boldsymbol{\kappa} - \frac{\mathbf{E}}{2}\tau_2 \right). \quad (\text{S26})$$

Since the lesser Green's function is written above as a double time integral, a full evaluation is not needed when one is interested only in the current rather than the complete spectral function. It is then sufficient to compute the equal-time lesser Green's function, which gives the momentum occupation:

$$\tilde{n}(\boldsymbol{\kappa}) = \text{Im} \tilde{G}^<(0, \boldsymbol{\kappa}). \quad (\text{S27})$$

Substituting Eq. (S26) with  $\tau = 0$ , we obtain

$$\tilde{n}(\boldsymbol{\kappa}) = \text{Im} \int d\tau_1 d\tau_2 \tilde{G}^R \left( \tau_1, \boldsymbol{\kappa} - \frac{\mathbf{E}}{2}\tau_1 \right) \Sigma^<(\tau_2 - \tau_1) \times \tilde{G}^A \left( -\tau_2, \boldsymbol{\kappa} - \frac{\mathbf{E}}{2}\tau_2 \right). \quad (\text{S28})$$

Using the steady-state relation

$$\tilde{G}^A(-\tau, \boldsymbol{\kappa}) = \tilde{G}^{R*}(\tau, \boldsymbol{\kappa}), \quad (\text{S29})$$

this expression can be rewritten as

$$\tilde{n}(\boldsymbol{\kappa}) = \text{Im} \int d\tau_1 d\tau_2 \tilde{G}^R \left( \tau_1, \boldsymbol{\kappa} - \frac{\mathbf{E}}{2}\tau_1 \right) \Sigma^<(\tau_2 - \tau_1) \times \tilde{G}^{R*} \left( \tau_2, \boldsymbol{\kappa} - \frac{\mathbf{E}}{2}\tau_2 \right). \quad (\text{S30})$$

For the constant bath considered here, the lesser self-energy takes the form

$$\Sigma^<(\tau_2 - \tau_1) = i\Gamma \int \frac{d\omega}{2\pi} e^{-i\omega(\tau_2 - \tau_1)} f(\omega), \quad (\text{S31})$$

where  $f(\omega)$  is the bath distribution function. Substituting this into Eq. (S30), one finds

$$\tilde{n}(\boldsymbol{\kappa}) = \text{Im} \int \frac{d\omega}{2\pi} (i\Gamma f(\omega)) \left[ \int d\tau_1 \tilde{G}^R \left( \tau_1, \boldsymbol{\kappa} - \frac{\mathbf{E}}{2}\tau_1 \right) e^{i\omega\tau_1} \right] \times \left[ \int d\tau_2 \tilde{G}^{R*} \left( \tau_2, \boldsymbol{\kappa} - \frac{\mathbf{E}}{2}\tau_2 \right) e^{-i\omega\tau_2} \right]. \quad (\text{S32})$$

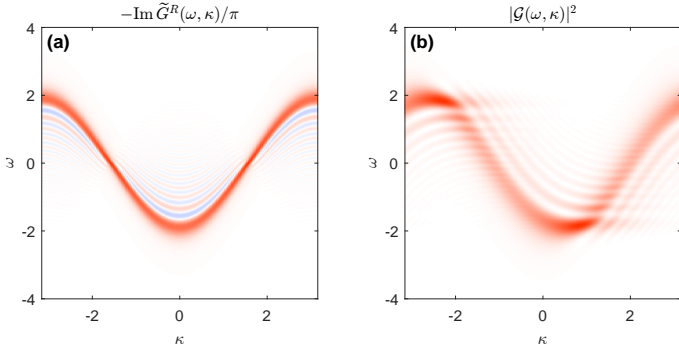


FIG. S1. Momentum- and frequency-resolved spectra for  $E = \Gamma = 0.1$ . (a) Wigner spectral function  $-\text{Im} \tilde{G}^R(\omega, \kappa)/\pi$ . (b) Field-dressed weight  $|\mathcal{G}(\omega, \kappa)|^2$ .

This motivates the definition of an effective spectral amplitude,

$$\mathcal{G}(\omega, \kappa) = \int_0^\infty d\tau \tilde{G}^R\left(\tau, \kappa - \frac{\mathbf{E}}{2}\tau\right) e^{i\omega\tau}, \quad (\text{S33})$$

in terms of which the occupation can be written in the compact form

$$\tilde{n}(\kappa) = \Gamma \int \frac{d\omega}{2\pi} f(\omega) |\mathcal{G}(\omega, \kappa)|^2. \quad (\text{S34})$$

To clarify the difference between Eq. (S33) and the Wigner Green's function in Eq. (S23), we compare them for a one-dimensional tight-binding model with  $\Gamma = E = 0.1$  in Fig. S1. Both the Wigner spectral function  $-\text{Im} \tilde{G}^R(\omega, \kappa)/\pi$  and the effective spectral weight  $|\mathcal{G}(\omega, \kappa)|^2$  develop field-induced oscillatory structures. The Wigner spectral function remains symmetric with respect to  $\kappa = 0$  in this model, but can take locally negative values because it is a quasi-distribution in Wigner space. In contrast,  $|\mathcal{G}(\omega, \kappa)|^2$  is positive by construction and becomes asymmetric with respect to  $\kappa = 0$ , reflecting how the field-driven momentum-space structure affects the occupation. It is therefore more directly connected to the nonequilibrium momentum distribution in Eq. (S34).

Once the occupation has been obtained, the current can be calculated by integrating the occupation weighted by the band velocity,

$$\mathbf{j} = q \int \frac{d^d \kappa}{(2\pi)^d} \mathbf{v}(\kappa) \tilde{n}(\kappa), \quad (\text{S35})$$

with

$$\mathbf{v}(\kappa) = \frac{1}{\hbar} \nabla_{\kappa} \epsilon(\kappa), \quad (\text{S36})$$

where  $d$  denotes the spatial dimension of the system.

#### Frequency-dependent self-energy

We next turn to the more general case of a frequency-dependent self-energy. This formulation is required when

considering a frequency-dependent bath, phonon coupling, or interaction-induced self-energy corrections. In this case, the simplifications used in the constant-damping approximation are no longer applicable, and the calculation must be carried out in terms of explicit multiple time integrals. In particular, Eq. (S1) for the retarded component becomes an integro-differential equation in the time domain. We therefore rewrite it in the iterative form

$$\tilde{G}^R(\tau, \kappa) = \tilde{G}_0^R(\tau, \kappa) + (\tilde{G}_0^R \star \Delta\Sigma^R \star \tilde{G}^R)(\tau, \kappa), \quad (\text{S37})$$

where  $\tilde{G}_0^R$  denotes the field-dressed propagator in the absence of the frequency-dependent correction  $\Delta\Sigma^R$ . It is obtained from Eq. (S23) by setting  $\Gamma = 0$ . Here  $\Delta\Sigma^R$  represents the self-energy correction arising from a frequency-dependent bath, phonons, or interactions.

To evaluate the triple product in Eq. (S37), we proceed in two steps and define

$$M(\tau, \kappa) \equiv (\Delta\Sigma^R \star \tilde{G}^R)(\tau, \kappa), \quad (\text{S38})$$

and

$$\text{corr}(\tau, \kappa) \equiv (\tilde{G}_0^R \star M)(\tau, \kappa), \quad (\text{S39})$$

so that the Dyson equation becomes

$$\tilde{G}^R(\tau, \kappa) = \tilde{G}_0^R(\tau, \kappa) + \text{corr}(\tau, \kappa). \quad (\text{S40})$$

Since  $\Delta\Sigma^R$  is assumed to be independent of  $\kappa$ , the first star product can be written, using Eq. (S24), as

$$M(\tau, \kappa) = \int_0^\tau d\tau_1 \Delta\Sigma^R(\tau_1) \tilde{G}^R\left(\tau - \tau_1, \kappa - \frac{\mathbf{E}}{2}\tau_1\right). \quad (\text{S41})$$

The field-induced shift is only along the electric-field direction. We therefore perform the Fourier expansion along this direction. Introducing

$$\kappa_{\parallel} = \hat{\mathbf{E}} \cdot \kappa, \quad \hat{\mathbf{E}} = \frac{\mathbf{E}}{|\mathbf{E}|}, \quad (\text{S42})$$

and denoting the remaining momentum components by  $\kappa_{\perp}$ , we expand

$$\tilde{G}^R(\tau, \kappa) = \sum_n e^{in\kappa_{\parallel}} \tilde{G}_n^R(\tau, \kappa_{\perp}), \quad (\text{S43})$$

and similarly

$$M(\tau, \kappa) = \sum_n e^{in\kappa_{\parallel}} M_n(\tau, \kappa_{\perp}). \quad (\text{S44})$$

Then

$$\begin{aligned} & \tilde{G}^R\left(\tau - \tau_1, \kappa - \frac{\mathbf{E}}{2}\tau_1\right) \\ &= \sum_n e^{in\kappa_{\parallel}} e^{-in|\mathbf{E}|\tau_1/2} \tilde{G}_n^R(\tau - \tau_1, \kappa_{\perp}), \end{aligned} \quad (\text{S45})$$

so that each harmonic satisfies an independent causal convolution,

$$M_n(\tau, \boldsymbol{\kappa}_\perp) = \int_0^\tau d\tau_1 K_n(\tau_1) \tilde{G}_n^R(\tau - \tau_1, \boldsymbol{\kappa}_\perp), \quad (\text{S46})$$

with

$$K_n(\tau_1) \equiv \Delta \Sigma^R(\tau_1) e^{-in|\mathbf{E}|\tau_1/2}. \quad (\text{S47})$$

Thus, the first star product is reduced to an ordinary causal convolution in time for each harmonic channel along the field direction. On a uniform grid  $\tau_m = m\Delta\tau$ , this convolution becomes

$$(M_n)_m = \Delta\tau \sum_{m'=0}^m (K_n)_{m'} (\tilde{G}_n)_{m-m'}. \quad (\text{S48})$$

Numerically, this convolution is evaluated using a zero-padded fast Fourier transform (FFT), and  $M(\tau, \boldsymbol{\kappa})$  is then reconstructed by an inverse FFT along the  $\kappa_\parallel$  direction.

The second star product is more involved, because both functions depend on  $\tau$  and  $\boldsymbol{\kappa}$ . Consequently, a fixed harmonic channel of the final result receives contributions from different combinations of harmonic channels of  $\tilde{G}_0^R$  and  $M$ , and the product no longer reduces to independent one-dimensional convolutions which can be calculated using FFT. Explicitly, the correction term is

$$\begin{aligned} \text{corr}(\tau, \boldsymbol{\kappa}) &= \int_0^\tau d\tau_2 \tilde{G}_0^R\left(\tau_2, \boldsymbol{\kappa} + \frac{\mathbf{E}}{2}(\tau - \tau_2)\right) \\ &\quad \times M\left(\tau - \tau_2, \boldsymbol{\kappa} - \frac{\mathbf{E}}{2}\tau_2\right). \end{aligned} \quad (\text{S49})$$

We evaluate this integral by direct summation on the discrete time grid. The momentum shifts are implemented spectrally rather than by interpolation, using the same idea as in Eq. (S45). For a periodic function along the field direction,

$$f(\kappa_\parallel) = \sum_n e^{in\kappa_\parallel} f_n, \quad (\text{S50})$$

one has

$$f(\kappa_\parallel + s) = \sum_n e^{in\kappa_\parallel} (e^{ins} f_n). \quad (\text{S51})$$

Thus each required shift along  $\mathbf{E}$  is implemented as

$$\{f(\kappa_{\parallel,j})\}_j \xrightarrow{\text{FFT}} \{f_n\}_n \longrightarrow \{e^{ins} f_n\}_n \xrightarrow{\text{IFFT}} \{f(\kappa_{\parallel,j+s})\}_j. \quad (\text{S52})$$

This procedure preserves periodicity along the field direction and avoids interpolation errors.

The Dyson equation is then solved iteratively, starting from the initial guess

$$\tilde{G}^R(\tau, \boldsymbol{\kappa}) = \tilde{G}_0^R(\tau, \boldsymbol{\kappa}), \quad (\text{S53})$$

and updating the solution through Eq. (S40). In practice, linear mixing is applied after each iteration to improve numerical stability and convergence.

The lesser Green's function with a frequency-dependent self-energy can be treated in a closely analogous manner. For the lesser component, the star-product expression in Eq. (S26) contains the same type of triple product as in the retarded Dyson equation. We therefore evaluate it in two steps, following the same strategy as for the retarded component. We first define

$$L(\tau, \boldsymbol{\kappa}) \equiv (\Sigma^< \star \tilde{G}^A)(\tau, \boldsymbol{\kappa}), \quad (\text{S54})$$

and then compute

$$\tilde{G}^<(\tau, \boldsymbol{\kappa}) = (\tilde{G}^R \star L)(\tau, \boldsymbol{\kappa}). \quad (\text{S55})$$

The numerical strategy is the same as for the retarded component. Since  $\Sigma^<$  is assumed to be independent of  $\boldsymbol{\kappa}$ , the first star product can again be reduced to independent convolutions in the  $\kappa_\parallel$ -harmonic representation and accelerated by FFT. The second star product is evaluated by direct summation, with the momentum shifts implemented spectrally as described above. The main difference from the retarded case is the time domain on which the functions are defined. Retarded and advanced quantities have causal support only on the positive and negative time branches, respectively, whereas  $\tilde{G}^<(\tau, \boldsymbol{\kappa})$  and  $\Sigma^<(\tau)$  are defined on the full relative-time interval. Therefore, the numerical implementation of the lesser component must be carried out on the full time grid rather than only on the causal half axis.

## WEAK-FIELD COMPARISON BETWEEN CONSTANT RELAXATION TIME AND CONSTANT SCATTERING RATE

In this section we clarify the difference between the commonly used constant relaxation-time approximation and the constant scattering-rate approximation used in our NEGF calculation. Although the two descriptions are often identified in studies of linear transport, they lead to different momentum-space distortions of the distribution, which becomes important when estimating the onset of the nonperturbative regime.

For simplicity, we consider a one-dimensional single-band problem with the electric field applied along the momentum coordinate  $\kappa$ . Starting from the effective spectral amplitude defined in Eq. (S33) and the occupation formula in Eq. (S34), the weak-field expansion of the spectral amplitude gives

$$\mathcal{G}(\omega, \kappa) = \mathcal{G}_0(\omega, \kappa) - iEv_\kappa \mathcal{G}_0^3(\omega, \kappa) + O(E^2), \quad (\text{S56})$$

where

$$\mathcal{G}_0(\omega, \kappa) = \frac{1}{\omega - \epsilon_\kappa + i\Gamma}, \quad v_\kappa = \partial_\kappa \epsilon_\kappa. \quad (\text{S57})$$

Substituting Eq. (S56) into Eq. (S34), the first-order correction to the occupation is

$$\delta \tilde{n}_\Gamma(\kappa) = -4E\Gamma^2 v_\kappa \int \frac{d\omega}{2\pi} f(\omega) \frac{\omega - \epsilon_\kappa}{[(\omega - \epsilon_\kappa)^2 + \Gamma^2]^3}. \quad (\text{S58})$$

At zero temperature,  $f(\omega) = \theta(\mu - \omega)$ . Using integration by parts, Eq. (S58) can be rewritten as

$$\delta\tilde{n}_\Gamma(\kappa) = -E\Gamma^2 v_\kappa \int \frac{d\omega}{2\pi} \frac{f'(\omega)}{[(\omega - \epsilon_\kappa)^2 + \Gamma^2]^2}. \quad (\text{S59})$$

Since  $f'(\omega) = -\delta(\omega - \mu)$ , this gives

$$\delta\tilde{n}_\Gamma(\kappa) = \frac{E\Gamma^2 v_\kappa}{2\pi [(\mu - \epsilon_\kappa)^2 + \Gamma^2]^2}. \quad (\text{S60})$$

The zero-field occupation obtained from Eq. (S34) is

$$\tilde{n}_0(\kappa) = \frac{1}{2\pi} \left[ \arctan \frac{\mu - \epsilon_\kappa}{\Gamma} + \frac{\pi}{2} \right], \quad (\text{S61})$$

and hence

$$\partial_\kappa \tilde{n}_0(\kappa) = -\frac{\Gamma v_\kappa}{2\pi [(\mu - \epsilon_\kappa)^2 + \Gamma^2]}. \quad (\text{S62})$$

Combining Eqs. (S60) and (S62), we obtain the exact first-order relation

$$\delta\tilde{n}_\Gamma(\kappa) = -\frac{E\Gamma}{(\mu - \epsilon_\kappa)^2 + \Gamma^2} \partial_\kappa \tilde{n}_0(\kappa). \quad (\text{S63})$$

Equivalently,

$$\tilde{n}_\Gamma(\kappa) = \tilde{n}_0(\kappa) - \Delta\kappa_\Gamma(\kappa) \partial_\kappa \tilde{n}_0(\kappa), \quad (\text{S64})$$

with the momentum-dependent effective displacement

$$\Delta\kappa_\Gamma(\kappa) = \frac{E\Gamma}{(\mu - \epsilon_\kappa)^2 + \Gamma^2}. \quad (\text{S65})$$

The displacement is largest at the Fermi surface,

$$\Delta\kappa_\Gamma = \frac{E}{\Gamma} \quad (\epsilon_\kappa = \mu), \quad (\text{S66})$$

and rapidly decreases away from it. A closely related weak-field analysis for an electric-field-driven tight-binding lattice coupled to fermion reservoirs was given in Ref. [55]. In that work, the field-induced displacement of the distribution near the Fermi surface reduces to the estimate  $\Delta k \sim E/\Gamma$ .

This result should be contrasted with the constant relaxation-time approximation. In that case, the distribution is assumed to be rigidly shifted by

$$\Delta\kappa_{\tau_B} = E\tau_B, \quad (\text{S67})$$

so that

$$\tilde{n}_{\tau_B}(\kappa) \simeq \tilde{n}_0(\kappa) - E\tau_B \partial_\kappa \tilde{n}_0(\kappa). \quad (\text{S68})$$

Using the convention  $\tau_B = 1/(2\Gamma)$ , this gives a constant shift

$$\Delta\kappa_{\tau_B} = \frac{E}{2\Gamma}. \quad (\text{S69})$$

The difference between the two approximations can be quantified by comparing the exact weak-field correction in Eq. (S63)

with the rigid-shift result in Eq. (S68). For  $\tau_B = 1/(2\Gamma)$ , their ratio is

$$\frac{\delta\tilde{n}_\Gamma(\kappa)}{\delta\tilde{n}_{\tau_B}(\kappa)} = \frac{2\Gamma^2}{(\mu - \epsilon_\kappa)^2 + \Gamma^2}. \quad (\text{S70})$$

This comparison also clarifies an important point. A constant scattering rate does not in general generate a rigidly shifted Fermi distribution. The constant scattering-rate result is twice as large as the matched relaxation-time result at the Fermi surface, but is strongly suppressed away from the Fermi surface. In other words, within the weak-field expansion, the effective shift in the constant scattering-rate approximation varies from its maximal value  $E/\Gamma$  at  $\epsilon_\kappa = \mu$  to nearly zero for  $|\epsilon_\kappa - \mu| \gg \Gamma$ . A simple heuristic estimate of the effective shift is therefore obtained by averaging these two limiting values,

$$\frac{1}{2} \left( 0 + \frac{E}{\Gamma} \right) = \frac{E}{2\Gamma}, \quad (\text{S71})$$

which coincides with the rigid shift in the constant relaxation-time approximation. In this sense, although the two approximations are not equivalent point by point in  $\kappa$ , they lead to the same characteristic displacement scale in the small- $\Gamma$  and weak-field limit.

This distinction between both approximations is unimportant in the strict weak-field limit if only the overall linear conductivity is considered. However, it becomes important for estimating the field scale at which the nonperturbative regime starts. In the constant relaxation-time approximation, all occupied states are shifted by the same amount  $E\tau_B$ . In the constant scattering-rate approximation, the relevant Fermi-surface displacement is instead  $E/\Gamma$ . Therefore, a criterion based on the Fermi-contour edge reaching a Berry-curvature hot spot [30] predicts a smaller crossover field in the constant scattering-rate description. This explains why a rigid-shift Berry-curvature-dipole estimate can reproduce the weak-field trend but predict a different nonperturbative crossover.

We finally note that the constant- $\Gamma$  model is a single-particle dissipative description and does not include an electron-electron collision integral. Fast electron-electron scattering may drive the system closer to a locally thermal, or hot-electron, distribution, thereby reducing the detailed k-dependent displacement found in the constant- $\Gamma$  model. The present comparison should therefore be viewed as contrasting two limiting weak-field descriptions: a rigid constant- $\tau$  shift and a reservoir-induced constant- $\Gamma$  nonthermal distribution.

## STRONG-FIELD MOMENTUM DISTRIBUTIONS

In the main text, we focused on the perturbative regime and on the onset of the nonperturbative regime in the momentum distribution  $\tilde{n}(\kappa)$ , where the field-driven drift can still be estimated from the scale  $E/\Gamma$ . Here we show additional momentum-space occupations at larger fields. These results illustrate the far-from-perturbative regime, where the simple

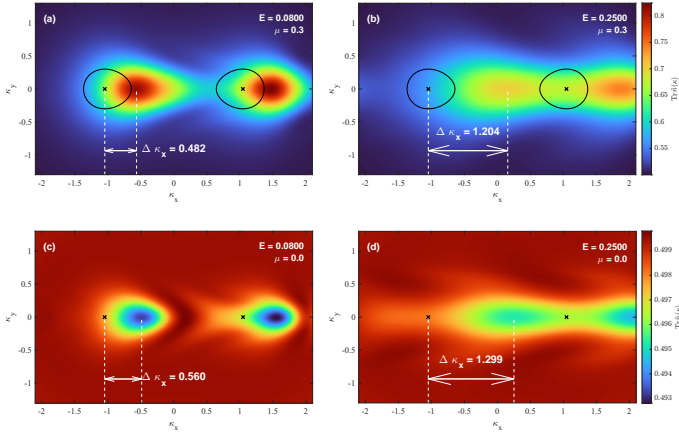


FIG. S2. Momentum-resolved occupation distribution  $\text{Tr} \tilde{n}(\boldsymbol{\kappa})$  in the strong-field regime. (a,b) Results for  $\mu = 0.3$  at  $E = 0.08$  and  $E = 0.25$ , respectively. (c,d) Results for  $\mu = 0$  at  $E = 0.08$  and  $E = 0.25$ , respectively. Black crosses mark the Weyl-like points, and black contours in (a,b) indicate the equilibrium Fermi surface for  $\mu = 0.3$ . White dashed lines and arrows denote the displacement  $\Delta \kappa_x$  of the occupation maximum or minimum along the  $\kappa_y \simeq 0$  line relative to the left Weyl-like point.

drift picture and the Berry-curvature-dipole interpretation are no longer sufficient.

Figure S2 shows the momentum distributions for two representative chemical potentials,  $\mu = 0.3$  and  $\mu = 0$ , at large fields  $E = 0.08$  and  $E = 0.25$ . The imaginary part of the self-energy for the bath is  $\Gamma = 0.1$ . For both chemical potentials, increasing the field leads to a more broadly redistributed occupation in momentum space. The maxima and minima associated with the Weyl-like-point structures are displaced farther away from the Weyl-like points, but the displacement no longer follows the simple estimate  $E/\Gamma$ . In the panels we indicate the distance between the left Weyl-like point and the nearby left peak. In the strong-field regime this distance is substantially smaller than  $E/\Gamma$ ; for example, at  $E = 0.25$  it is only about half of the naive drift estimate. Moreover, increasing the field further does not lead to a proportional increase of the displacement. This indicates that the momentum-space drift saturates and that the simple drift picture breaks down in the far-from-perturbative regime.

Additional features also emerge at large fields. First, the drift distances of the left and right structures are not identical. This reflects the fact that the band structure on the two sides of the Weyl-like points is not symmetric, so the field-induced redistribution depends on the local dispersion rather than only on the ratio  $E/\Gamma$ . Second, the amplitudes of the left and right extrema become unequal, especially at  $E = 0.25$ , where the left feature is significantly weaker than the right one. These asymmetries show that the strong-field distribution cannot be understood in terms of a rigidly shifted weak-field pattern.

The semimetallic case  $\mu = 0$  displays an additional complication. At  $E = 0.08$ , the oscillatory tail of the hole-like structure generated near the left Weyl-like point extends toward

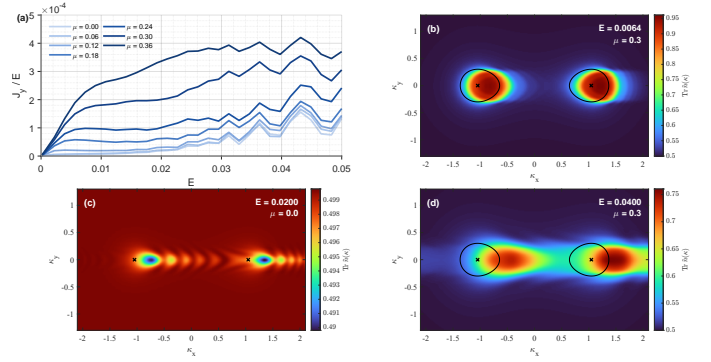


FIG. S3. Results for a smaller scattering rate  $\Gamma = 0.02$ . (a) Field-normalized transverse current  $J_y/E$  as a function of the driving field  $E$  for several chemical potentials  $\mu$ . (b)–(d) Momentum-space occupation maps  $\text{Tr} \tilde{n}(\boldsymbol{\kappa})$  at representative fields. Panels (b) and (d) show results for  $\mu = 0.30$ , with the upper-band Fermi contour and the Weyl-like points indicated. Panel (c) shows the result for the case  $\mu = 0.00$  at  $E = 0.02$ , with the Weyl-like points marked.

the structure associated with the right Weyl-like point. Thus the nonequilibrium structures generated near the two Weyl-like points begin to overlap and influence each other. This overlap makes the field dependence of the Hall response more complex and contributes to the nonmonotonic, strongly non-perturbative behavior discussed in the main text.

## ROBUSTNESS AGAINST A SMALLER SCATTERING RATE

In the main text, we mainly use the damping rate  $\Gamma = 0.1$ . This value is convenient numerically, since it allows to compute the nonequilibrium steady state within a moderate time and on a manageable momentum grid. In clean metallic or semimetallic samples, however, the effective momentum scattering rate can be substantially smaller. For example, terahertz measurements on the Dirac semimetal  $\text{Cd}_3\text{As}_2$  reported a momentum scattering time of about 157 fs [56]. To compare this value with the dimensionless damping in the lattice model, we estimate

$$\frac{\Gamma}{\hbar v_F/a} \sim \frac{a}{v_F \tau}, \quad (\text{S72})$$

up to a convention-dependent factor of order unity. Using  $v_F \sim 1.5 \times 10^6$  m/s [57] and  $a \simeq 12.6$  Å [58], this gives

$$\frac{a}{v_F \tau} \sim 10^{-2}. \quad (\text{S73})$$

In our lattice model, the lattice constant and the Dirac velocity are both of order unity, so that  $\Gamma/(\hbar v_F/a)$  is of the same order as the damping parameter  $\Gamma$ . This estimate indicates that clean  $\text{Cd}_3\text{As}_2$  corresponds to a rather weak-damping regime of the lattice model. It is therefore useful to check whether the nonperturbative features discussed in the main text remain visible at weaker damping.

Figure S3(a) shows the field dependence of  $J_y/E$  for  $\Gamma = 0.02$  with different chemical potentials, corresponding to the results of Fig. 1(b) in the main text. The overall structure remains the same: the weak-field response follows the perturbative scaling, while deviations appear once the field-driven distribution reaches the relevant Berry-curvature hot spots. The main effect of reducing  $\Gamma$  is to shift the crossover fields to smaller values and to make the nonperturbative features sharper. This behavior is consistent with the drift estimate  $\Delta\kappa_x \sim E/\Gamma$ , which implies that a smaller field is needed to produce the same momentum-space displacement when the damping is reduced.

Figures S3(b)–S3(d) show the corresponding momentum-space occupations  $\text{Tr} \tilde{n}(\boldsymbol{\kappa})$  for representative cases, analogous to Fig. 2 in the main text and Fig. S2. Figure S3(b) shows the result for  $\mu = 0.3$  and  $E = 0.0064$ . According to the simple drift estimate  $\Delta\kappa_x \sim E/\Gamma$ , this field corresponds to a displacement comparable to the distance between the Fermi contour edge and the Weyl-like point. One might therefore expect, by analogy with Fig. 2, that the edge of the high-occupation region is shifted to the Weyl-like point. The actual distribution in Fig. S3(b), however, is more subtle. Although a narrow line-like structure appears near the Weyl-like point, the boundary of the high-occupation region still encloses it, rather than being simply displaced to it. This behavior is a consequence of the constant-scattering-rate approximation. As shown in Eq. (S65), the effective displacement is energy dependent: it is maximal at the Fermi surface, where it equals  $E/\Gamma$ , and decreases rapidly away from the chemical potential. For smaller  $\Gamma$ , this decrease becomes sharper, so that essentially only the outermost layer of the broadened Fermi edge is shifted by the full amount  $E/\Gamma$ . The total occupation edge therefore does not behave as a rigidly shifted contour and need not coincide with the Weyl-like point. Nevertheless, Fig. S3(a) shows that the same field scale still coincides well with the turning point of the Hall response. This confirms that the onset of the nonperturbative feature is controlled by the displacement of the Fermi-surface layer, rather than by the apparent boundary of the full momentum occupation.

Figure S3(c) shows the semimetallic case  $\mu = 0$  at  $E = 0.02$ . Compared with the corresponding  $\Gamma = 0.1$  distributions discussed above, the oscillatory structures are more pronounced, as expected from the weaker damping. Finally, Fig. S3(d) shows the case with  $\mu = 0.3$  at  $E = 0.04$ , already in the deep nonperturbative regime. The overall structure is consistent with the strong-field distributions shown in Fig. S2, but the momentum displacement has a smaller saturated drift.

Overall, these smaller- $\Gamma$  results show that the energy-dependent effective drift in the constant- $\Gamma$  approximation becomes more important for the detailed momentum-space structure when damping is weak. Nevertheless, the main nonperturbative features identified in the main text remain robust, indicating that our conclusions are also relevant for cleaner materials with smaller scattering rates.

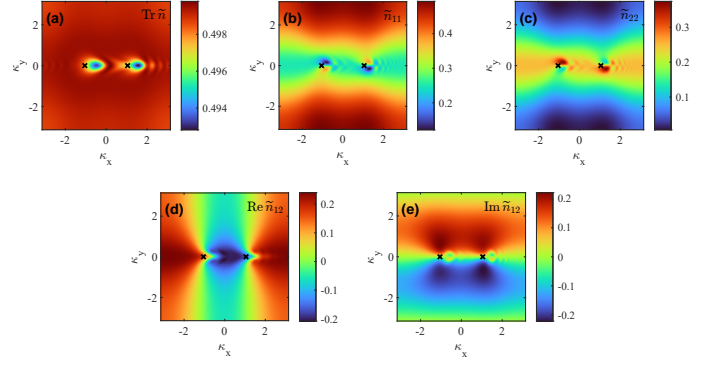


FIG. S4. Momentum-resolved density matrix in the orbital basis for the case with  $\mu = 0$  and  $\Gamma = 0.1$  at driving field  $E = 0.08$ . The panels show the trace of the occupation matrix,  $\text{Tr} \tilde{n}(\boldsymbol{\kappa}) = \tilde{n}_{11}(\boldsymbol{\kappa}) + \tilde{n}_{22}(\boldsymbol{\kappa})$  (a), together with the orbital-basis matrix elements  $\tilde{n}_{11}$  (b),  $\tilde{n}_{22}$  (c),  $\text{Re} \tilde{n}_{12}$  (d), and  $\text{Im} \tilde{n}_{12}$  (e). Black crosses mark the positions of the two Weyl-like points.

### MOMENTUM-RESOLVED DENSITY MATRIX IN DIFFERENT BASES

In the main text, we visualize the nonequilibrium momentum distribution through the total occupation  $\text{Tr} \tilde{n}(\boldsymbol{\kappa}) = \tilde{n}_{11}(\boldsymbol{\kappa}) + \tilde{n}_{22}(\boldsymbol{\kappa})$ , as shown in Fig. 2. This quantity is basis independent and contains the combined contribution from the two orbital components, or from the upper and lower bands. To gain more microscopic insight, we further decompose the momentum-resolved density matrix into its individual matrix elements in different bases. This analysis is particularly useful for the semimetal case  $\mu = 0$ , where the Hall response is governed by interband charge transfer rather than by a conventional Fermi-surface drift.

We first analyze the density matrix in the original orbital basis, i.e., the basis in which the Hamiltonian in the main text is written. As a representative example, we choose  $\mu = 0$ ,  $E = 0.08$ , and  $\Gamma = 0.1$ . The corresponding momentum-resolved matrix elements are shown in Fig. S4. Since the density matrix is Hermitian, we only show the real parts of the two diagonal elements,  $\text{Re} \tilde{n}_{11}(\boldsymbol{\kappa})$  and  $\text{Re} \tilde{n}_{22}(\boldsymbol{\kappa})$ , together with the real and imaginary parts of the off-diagonal element,  $\text{Re} \tilde{n}_{12}(\boldsymbol{\kappa})$  and  $\text{Im} \tilde{n}_{12}(\boldsymbol{\kappa})$ . For comparison, the total occupation  $\text{Tr} \tilde{n}(\boldsymbol{\kappa})$  is also displayed.

The two diagonal orbital components have distinct momentum-space distributions. The first orbital mainly contributes to the occupation near  $\kappa_y = \pi$ , whereas the second orbital mainly contributes near  $\kappa_y = 0$ . Under the applied electric field, pronounced nonequilibrium structures are generated around the Weyl-like points. These structures are visible not only in the diagonal components but also in both the real and imaginary parts of the off-diagonal density matrix. Another feature is that the total occupation  $\text{Tr} \tilde{n}(\boldsymbol{\kappa})$  remains symmetric with respect to  $\kappa_y = 0$ , while the individual orbital occupations  $\tilde{n}_{11}(\boldsymbol{\kappa})$  and  $\tilde{n}_{22}(\boldsymbol{\kappa})$  do not separately exhibit this symmetry.

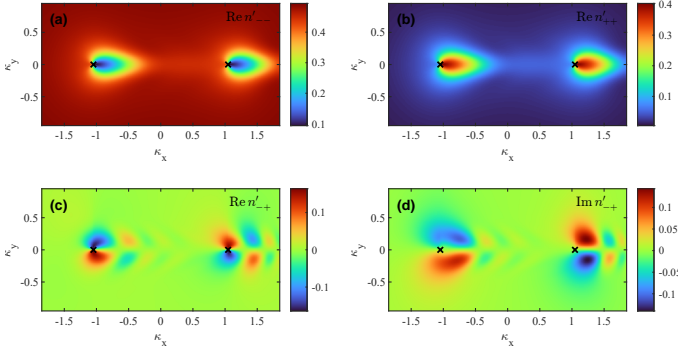


FIG. S5. Momentum-resolved density matrix in the diagonalized basis for the model with  $\mu = 0$  and  $\Gamma = 0.1$  at driving field  $E = 0.08$ . The panels show the trace of the occupation matrix elements  $n'_{--}$  (a),  $n'_{++}$  (b),  $\text{Re } n'_{-+}$  (c), and  $\text{Im } n'_{-+}$  (d). Black crosses mark the positions of the two Weyl-like points.

Although the orbital-basis decomposition already reveals the structure of the density matrix, it is not the most intuitive representation for discussing interband charge transfer. It is therefore useful to transform the density matrix to the equilibrium band basis, i.e., the basis that diagonalizes the field-free Hamiltonian,

$$U^\dagger(\boldsymbol{\kappa})H(\boldsymbol{\kappa})U(\boldsymbol{\kappa}) = \begin{pmatrix} \varepsilon_-(\boldsymbol{\kappa}) & 0 \\ 0 & \varepsilon_+(\boldsymbol{\kappa}) \end{pmatrix}. \quad (\text{S74})$$

The density matrix in this basis is

$$n'(\boldsymbol{\kappa}) = U^\dagger(\boldsymbol{\kappa})\tilde{n}(\boldsymbol{\kappa})U(\boldsymbol{\kappa}). \quad (\text{S75})$$

In equilibrium,  $n'(\boldsymbol{\kappa})$  is diagonal in the equilibrium band basis, where the  $+$  and  $-$  states denote the eigenstates of the field-free Hamiltonian. In other words, the off-diagonal matrix elements vanish at  $E = 0$  only after transforming to this  $+/-$  basis. This makes the field-induced interband coherence directly visible. For the semimetallic case  $\mu = 0$  considered here, the equilibrium state is close to a filled lower band and an empty upper band in the small- $\Gamma$  limit, up to spectral-broadening effects near the Weyl-like points. The field-induced changes of the diagonal populations and off-diagonal coherences are therefore especially transparent in the equilibrium band basis.

In performing the transformation in Eq. (S75), one has to fix the gauge of the eigenvectors at different momenta. A direct diagonalization at each  $\boldsymbol{\kappa}$  point leaves an arbitrary momentum-dependent phase, which can make the off-diagonal element  $n'_{+-}(\boldsymbol{\kappa})$  appear artificially discontinuous. We therefore choose a smooth gauge by requiring the overlap between eigenvectors at neighboring  $\boldsymbol{\kappa}$  points to be real and positive. This procedure removes rapid phase jumps in momentum space, although an overall phase freedom remains.

The resulting band-basis density matrix is shown in Fig. S5. Since the trace is invariant under the unitary transformation,  $\text{Tr } n'(\boldsymbol{\kappa}) = \text{Tr } \tilde{n}(\boldsymbol{\kappa})$ , it is not plotted again. Figures S5(a) and S5(b) show the diagonal elements of  $n'(\boldsymbol{\kappa})$ , corresponding to

the lower- and upper-band occupations. Both are symmetric with respect to  $\kappa_y = 0$ . Unlike the hole-like structure in the total occupation, whose center is shifted away from the Weyl-like point, the strongest changes in the individual band occupations occur near the Weyl-like points themselves. This is expected, because the band gap vanishes there and interband charge transfer is most efficient. The shifted hole-like structure in  $\text{Tr } \tilde{n}(\boldsymbol{\kappa})$  therefore results from the imbalance between the field-induced lower- and upper-band population changes.

Figures S5(c) and S5(d) show the real and imaginary parts of the off-diagonal element  $n'_{+-}(\boldsymbol{\kappa})$ . These components measure the interband coherence in the equilibrium band basis. They are concentrated near the Weyl-like points, are not symmetric with respect to  $\kappa_y = 0$ , and exhibit oscillatory structures. These oscillations have the same origin as the oscillatory tails observed in the total occupation: they are generated by field-induced interband resonances near the cones. In the following, we will show that the Hall current originates entirely from the interband contribution.

In the band basis, the transverse current is

$$J_y = \int_{\text{BZ}} \frac{d^2\boldsymbol{\kappa}}{(2\pi)^2} \text{Tr} [v'_y(\boldsymbol{\kappa})n'(\boldsymbol{\kappa})], \quad (\text{S76})$$

where

$$v'_y(\boldsymbol{\kappa}) = U^\dagger(\boldsymbol{\kappa}) \partial_{\kappa_y} H(\boldsymbol{\kappa}) U(\boldsymbol{\kappa}). \quad (\text{S77})$$

Writing the band indices as  $-$  and  $+$ , this becomes

$$J_y = \int_{\text{BZ}} \frac{d^2\boldsymbol{\kappa}}{(2\pi)^2} [v'^y_{--}n'_{--} + v'^y_{++}n'_{++} + 2\text{Re}(v'^y_{+-}n'_{-+})]. \quad (\text{S78})$$

The diagonal velocity matrix elements are simply the band velocities,

$$v'^y_{\pm\pm}(\boldsymbol{\kappa}) = \partial_{\kappa_y} \varepsilon_{\pm}(\boldsymbol{\kappa}) = \pm \partial_{\kappa_y} \varepsilon(\boldsymbol{\kappa}), \quad (\text{S79})$$

with  $\varepsilon(\boldsymbol{\kappa}) = |\mathbf{d}(\boldsymbol{\kappa})|$ . For the model used in the main text,

$$\mathbf{d}(\boldsymbol{\kappa}) = ((\cos \kappa_x - D_x), \sin \kappa_y, (\cos \kappa_y - D_y)), \quad (\text{S80})$$

and hence

$$\partial_{\kappa_y} \varepsilon(\boldsymbol{\kappa}) = \frac{D_y \sin \kappa_y}{\varepsilon(\boldsymbol{\kappa})}, \quad (\text{S81})$$

which is odd under  $\kappa_y \rightarrow -\kappa_y$ . Since the diagonal occupations  $n'_{--}$  and  $n'_{++}$  are even in  $\kappa_y$ , their contributions to  $J_y$  vanish after integration over the Brillouin zone. Therefore, for the present symmetry setting, the transverse Hall current is carried by the off-diagonal term in Eq. (S78).

To further inspect how the off-diagonal density matrix generates the Hall current, we plot the momentum-resolved contribution of the last term in Eq. (S78). Its Brillouin-zone integral gives the total transverse current. We consider two representative parameter sets,  $(E, \mu) = (0.03, 0.3)$  and  $(E, \mu) = (0.08, 0)$ , shown in Figs. S6(a)–(c) and Figs. S6(d)–(f), respectively. The scattering rate is  $\Gamma = 0.1$ .

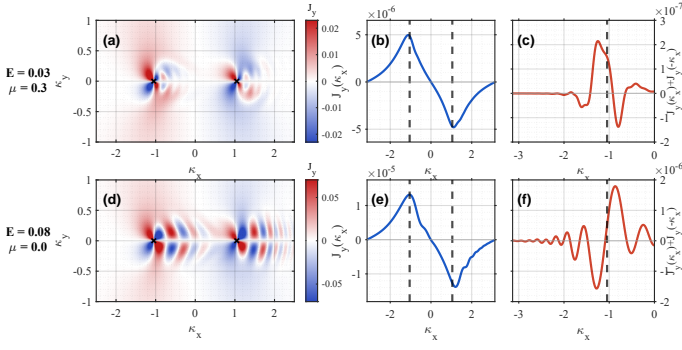


FIG. S6. Momentum-resolved off-diagonal contribution to the Hall current in the field-free band basis. The upper and lower rows correspond to  $(E, \mu) = (0.03, 0.3)$  and  $(0.08, 0.0)$ , respectively. Panels (a,d) show  $J_y(\kappa_x, \kappa_y)$ , panels (b,e) show the  $\kappa_y$ -integrated  $J_y(\kappa_x)$ , and panels (c,f) show  $J_y(\kappa_x) + J_y(-\kappa_x)$ . Vertical dotted lines mark the positions of Weyl-like points.

For each case, we first show the two-dimensional distribution  $J_y(\kappa)$ . We then integrate over  $\kappa_y$  to get  $J_y(\kappa_x)$ , and finally fold the positive and negative  $\kappa_x$  axes by plotting  $J_y(\kappa_x) + J_y(-\kappa_x)$ . This folded quantity highlights the residual imbalance between opposite momenta that survives the cancellation in the Brillouin-zone integral.

Although Eq. (S78) shows that the Hall current is carried by the off-diagonal term, Fig. S6 also demonstrates why a simple momentum-space picture analogous to the Berry-curvature-dipole interpretation is difficult to construct in the full Hall current calculation. The two-dimensional distributions in Figs. S6(a) and S6(d) are highly oscillatory. The net contribution can be attributed to the asymmetry after the  $\kappa_y$  integration in Figs. S6(b) and S6(e). But oscillations emerge again after folding the positive and negative  $\kappa_x$  axes in Figs. S6(c) and S6(f). The dominant contributions are concentrated around the Weyl-like points, but the net Hall current results from a delicate cancellation of oscillatory structures, making it difficult to assign the current to a single localized feature.

The semimetallic case  $\mu = 0$  shows an even cleaner oscillatory pattern than the finite-density case  $\mu = 0.3$ , with additional structures from an existing Fermi surface. As the electric field is increased, these oscillatory off-diagonal contributions become more pronounced. This provides a microscopic view of why the transverse current in the interband regime can develop a nonmonotonous nonperturbative field dependence.

### FIELD AND DAMPING DEPENDENCE OF THE INTERBAND MECHANISM

In the previous section, the density matrix in the equilibrium band basis revealed the interband character of the response in the semimetallic case  $\mu = 0$ . This interband contribution cannot be reliably captured by a quasiparticle anomalous-velocity formula based only on Berry curvature, and therefore lacks a simple Fermi-surface-shift interpreta-

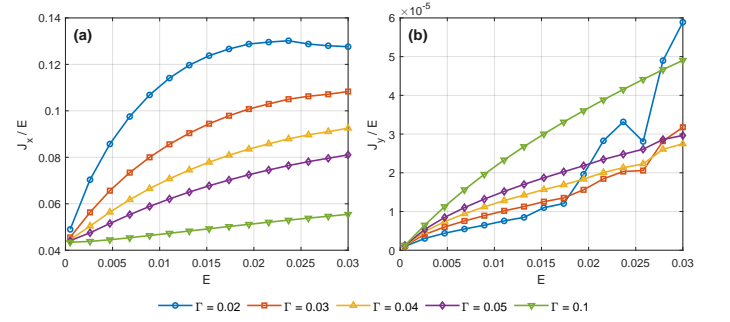


FIG. S7. Current response as a function of electric field  $E$  for different relaxation rates  $\Gamma$  when  $\mu = 0$ . (a) Longitudinal response  $J_x/E$ . (b) Transverse response  $J_y/E$ .

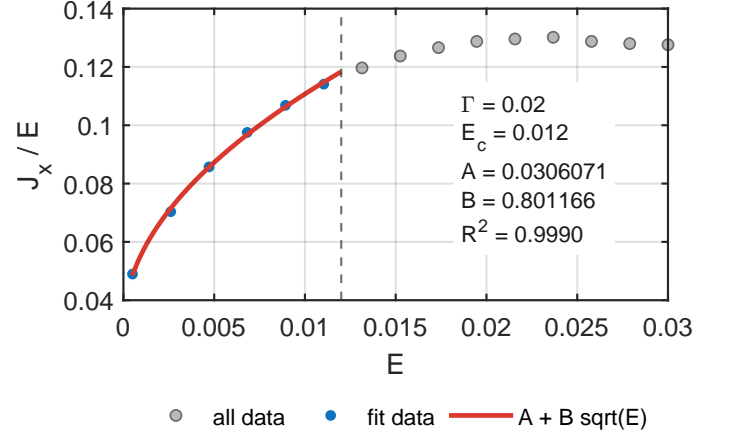


FIG. S8. Fit of the longitudinal current response of the semimetal case for  $\Gamma = 0.02$  in the weak-field regime. The data are fitted with  $J_x/E = A + B\sqrt{E}$  using points with  $E < E_c = 0.012$ .

tion. Here, we analyze how it depends on the electric field and on the damping rate  $\Gamma$ . This provides a complementary view of the interband charge-transfer process and clarifies the different behavior of the longitudinal and transverse currents.

Figure S7(a) shows the longitudinal conductivity  $\sigma_x = J_x/E$  for several values of  $\Gamma$ , while Fig. S7(b) shows the corresponding transverse response  $J_y/E$ . Interestingly, the two quantities show opposite trends with damping. The longitudinal conductivity decreases as  $\Gamma$  is increased, whereas the transverse response becomes larger. Their field dependences are also qualitatively different. The longitudinal conductivity has a finite intercept in the weak-field limit and then increases in a nonlinear fashion, while  $J_y/E$  has no intercept and grows approximately as a power  $\alpha < 1$  of the electric field.

We first discuss the longitudinal response. For the smallest damping rate considered here,  $\Gamma = 0.02$ , the weak-field behavior of  $\sigma_x$  is well described by

$$\sigma_x(E) = \frac{J_x(E)}{E} \simeq A + B\sqrt{E}, \quad (\text{S82})$$

as shown in Fig. S8. The constant term  $A$  represents the conductivity at the Dirac point in the weak-field limit. This

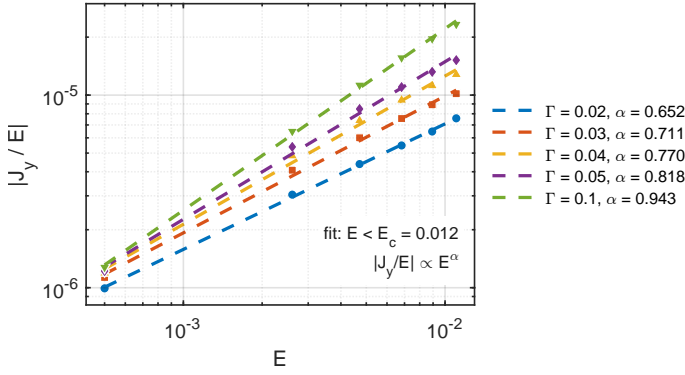


FIG. S9. Log-log scaling of the transverse current response  $|J_y/E|$  as a function of electric field  $E$  for different relaxation rates  $\Gamma$ . Dashed lines show power-law fits  $|J_y/E| \propto E^\alpha$  using the low-field data with  $E < E_c = 0.012$ . The fitted exponent  $\alpha$  is indicated in the legend for each  $\Gamma$ .

is analogous to the situation in graphene, where the dc response at the Dirac point contains an interband polarization contribution and cannot be interpreted simply as a Drude response from a Fermi surface [59, 60]. The  $\sqrt{E}$  correction can be understood as a signature of field-induced carrier production. For an ideal two-dimensional Dirac cone, the Schwinger mechanism gives a field-induced carrier excitation  $\Delta n(E) \propto E^{3/2}$ , as discussed for graphene in Refs. [60, 61]. These field-induced carriers then contribute to the longitudinal current in the presence of relaxation, which gives

$$\Delta J_x(E) \propto \frac{\Delta n(E)}{\Gamma} \propto \frac{E^{3/2}}{\Gamma}. \quad (\text{S83})$$

Consequently, for fixed  $\Gamma$ , the corresponding correction to the longitudinal conductivity scales as  $\sqrt{E}$ , consistent with the fit in Fig. S8. As  $\Gamma$  is increased, the field-induced current is reduced by faster relaxation, which explains why the finite-field correction to  $\sigma_x$  decreases with increasing damping. By contrast, the weak-field intercept is much less sensitive to  $\Gamma$ . This behavior is consistent with the interband contribution obtained from the Kubo formula at the Dirac point [59]. Although Ref. [60] studies the real-time dynamics of isolated graphene rather than a dissipative steady state, the separation between the weak-field interband contribution and the field-induced carrier-production contribution provides a useful interpretation of our results.

The transverse response is more difficult to interpret in terms of a simple quasiparticle picture. Figure S9 shows  $J_y/E$  on a log-log scale. Power-law fits in the weak-to-intermediate field regime give exponents  $\alpha$  in the range 0.6–0.9, indicating that the response is not simply linear in  $E$ . This nontrivial field dependence reflects the complex nature of the interband Hall response. In the interband regime, the electric field generates both electron-hole excitations and interband coherence near the cones.

For  $J_x/E$ , the weak-field intercept and the subsequent increase with field can be related to the interband Kubo contri-

bution and to field-induced carriers. These two contributions can be separated reasonably well in the perturbative regime. For  $J_y/E$ , however, the Hall response cannot be attributed only to interband carrier excitation, nor can it be reliably computed from a Berry-curvature-weighted band occupation. Instead, it depends on the full nonequilibrium density matrix. As a result, we do not expect a simple quasiparticle picture or a universal power law for  $J_y/E$  in this regime.

The damping dependence of the transverse response is also nontrivial. In the data shown in Fig. S9,  $J_y/E$  increases with increasing  $\Gamma$ , opposite to the trend of the longitudinal conductivity. A semiclassical Berry-curvature picture suggests one possible intuition: smaller  $\Gamma$  allows the field-induced structures to drift farther in momentum space, which can reduce their overlap with the Dirac-point hot spots. However, as shown in the main text, such a Berry-curvature-weighted occupation formula does not quantitatively reproduce the full NEGF current once interband processes becomes important. We therefore regard this picture only as a qualitative guide, not as a consistent explanation of the transverse current.

The results of our analysis show that the semimetallic response at  $\mu = 0$  is governed by field-induced interband charge transfer and coherence rather than by a conventional Fermi-surface drift. The field and damping dependences of  $J_x/E$  and  $J_y/E$  provide complementary diagnostics of this interband regime. While the longitudinal response admits a relatively simple interpretation in terms of interband carrier production and relaxation, the transverse Hall response depends on the full nonequilibrium density matrix and therefore has a more complex dependence on both  $E$  and  $\Gamma$ .

## EFFECTS FROM ELECTRON-PHONON COUPLING AND LOCAL INTERACTIONS

In the main text, we showed that electron-phonon coupling and local interactions can substantially modify the nonlinear Hall response. Here we describe how these effects are incorporated into the steady-state NEGF calculation and clarify their physical origin. In our framework, both effects enter through local self-energies. These self-energies affect the Hall response not only through their imaginary parts, which describe additional damping, but also through their real parts, which renormalize the effective band structure and hence the Berry-curvature distribution.

In the calculation, we start from the converged nonequilibrium Green's function of the noninteracting system coupled to the fermionic bath. This solution is then used as the initial input for a DMFT self-consistency loop. At each iteration, the local Green's function is computed as

$$G_{\text{loc}}(\omega) = \int_{\text{BZ}} \frac{d^2\kappa}{(2\pi)^2} \tilde{G}(\omega, \kappa), \quad (\text{S84})$$

and the electron-phonon or interaction self-energy is evaluated from this local Green's function. Since the local coupling considered here is orbital diagonal in the original orbital basis, the

resulting self-energy is diagonal in the same basis,

$$\Sigma(\omega) = \begin{pmatrix} \Sigma_{11}(\omega) & 0 \\ 0 & \Sigma_{22}(\omega) \end{pmatrix}. \quad (\text{S85})$$

This self-energy is inserted back into the lattice Dyson equation, and the process is repeated until convergence.

For the electron-phonon calculation, we use a local Holstein-type coupling to a local optical phonon mode of frequency  $\omega_0 = 1$ . The coupling strength is set to  $g = 0.3$ . Within the Migdal approximation, the diagonal components of the self-energy are given by

$$\Sigma_{\text{ph},aa}(t) = ig^2 D(t) G_{\text{loc},aa}(t), \quad a = 1, 2, \quad (\text{S86})$$

where  $D$  is the bare phonon propagator. The lesser component is

$$\Sigma_{\text{ph},aa}^<(t) = ig^2 D^<(t) G_{\text{loc},aa}^<(t), \quad (\text{S87})$$

and the retarded component is obtained by the Langreth rule,

$$\begin{aligned} \Sigma_{\text{ph},aa}^R(t) = ig^2 \left[ D^R(t) G_{\text{loc},aa}^<(t) + D^<(t) G_{\text{loc},aa}^R(t) \right. \\ \left. + D^R(t) G_{\text{loc},aa}^R(t) \right]. \end{aligned} \quad (\text{S88})$$

These expressions are evaluated self-consistently using the dressed local Green's function.

For the local interaction, we use a boldfied second-order perturbation theory with  $U = 0.8$  [51]. The second-order self-energy is evaluated from the dressed local Green's function. In terms of greater and lesser components, we use

$$\Sigma_{U,aa}^>(t) = U^2 \left[ G_{\text{loc},aa}^>(t) \right]^2 G_{\text{loc},aa}^<(-t), \quad (\text{S89})$$

and the retarded component is reconstructed as

$$\Sigma_{U,aa}^R(t) = \theta(t) \left[ \Sigma_{U,aa}^>(t) - \Sigma_{U,aa}^<(t) \right]. \quad (\text{S90})$$

This approximation captures the leading local interaction-induced spectral renormalization and damping effects, while remaining numerically affordable in the frequency-dependent steady-state calculation.

Figure S10(a) shows the real and imaginary parts of the two diagonal components of the interaction self-energy for the parameters used in the representative case of the main text: a Lorentzian fermionic bath with peak amplitude  $\Gamma = 0.1$  and half-width  $W = 4$ , at  $T = 1/30$  and  $\mu = 0.3$ , but here we set  $E = 0$ . The corresponding sum and difference are shown in Fig. S10(b). Figure S10(c) shows the analogous quantities for the electron-phonon self-energy, and Fig. S10(d) shows their sum and difference. The low-energy behavior is similar in the two cases. The real parts are sizable, while the imaginary parts remain relatively small in the low-energy window relevant for the Hall response. Thus, for these parameters, the low-energy broadening is still dominated by the fermionic bath damping, whose peak amplitude is  $\Gamma = 0.1$ , whereas the interaction and electron-phonon self-energies mainly affect the response

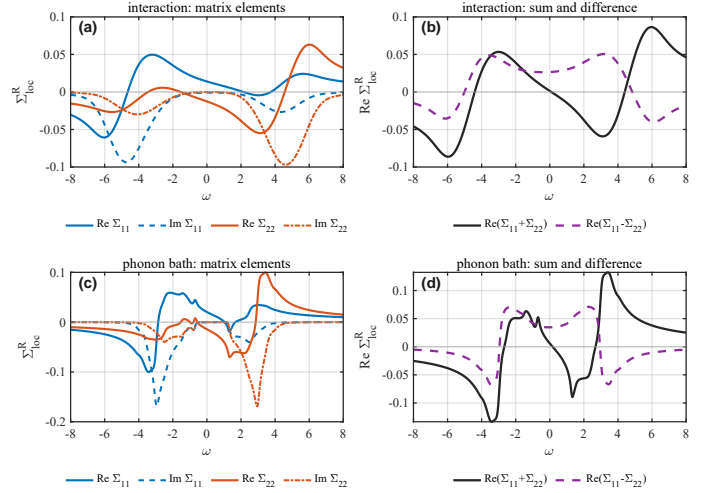


FIG. S10. Local retarded self-energies for the interaction and phonon-bath cases. (a,c) Real and imaginary parts of the diagonal matrix elements  $\Sigma_{11,\text{loc}}^R$  and  $\Sigma_{22,\text{loc}}^R$ . (b,d) Sum and difference of their real parts,  $\text{Re}(\Sigma_{11,\text{loc}}^R + \Sigma_{22,\text{loc}}^R)$  and  $\text{Re}(\Sigma_{11,\text{loc}}^R - \Sigma_{22,\text{loc}}^R)$ .

through their real parts. Since the results shown here are obtained at  $E = 0$ , they should be viewed as equilibrium reference self-energies for the nonequilibrium calculations. A finite electric field can in principle generate additional low-energy scattering in the driven steady state. For the phonon self-energy, the imaginary part is strongly suppressed in the window around the chemical potential bounded by the one-phonon threshold. For the interaction self-energy, the imaginary part is small but not strictly zero.

The real part of the diagonal self-energy can be decomposed into a symmetric and an antisymmetric part in orbital space,

$$\Sigma_0(\omega) = \frac{\Sigma_{11}(\omega) + \Sigma_{22}(\omega)}{2}, \quad \Sigma_z(\omega) = \frac{\Sigma_{11}(\omega) - \Sigma_{22}(\omega)}{2}. \quad (\text{S91})$$

The symmetric part  $\Sigma_0$  shifts both orbitals equally and therefore mainly produces an overall energy shift. It does not modify the Berry curvature. By contrast, the antisymmetric part  $\Sigma_z$  acts as an additional  $\sigma_z$  term. For the model used in the main text

$$d_z(\mathbf{k}) = (\cos k_y - D_y), \quad (\text{S92})$$

so the real part of  $\Sigma_z$  effectively renormalizes  $D_y$ . At low energy, this can be approximated by

$$D_y^{\text{eff}} = D_y - \text{Re} \Sigma_z^R(\omega = 0). \quad (\text{S93})$$

A positive value of  $\text{Re} \Sigma_{11}^R(0) - \text{Re} \Sigma_{22}^R(0)$  therefore reduces the effective  $D_y$ , opens a small gap near the Weyl-like points, and modifies the Berry-curvature hot spots. We have demonstrated this point in the main text.

To verify this interpretation further, we compare the full self-consistent calculation with an effective noninteracting calculation in which  $D_y$  is replaced by  $D_y^{\text{eff}}$ . The value of  $D_y^{\text{eff}}$

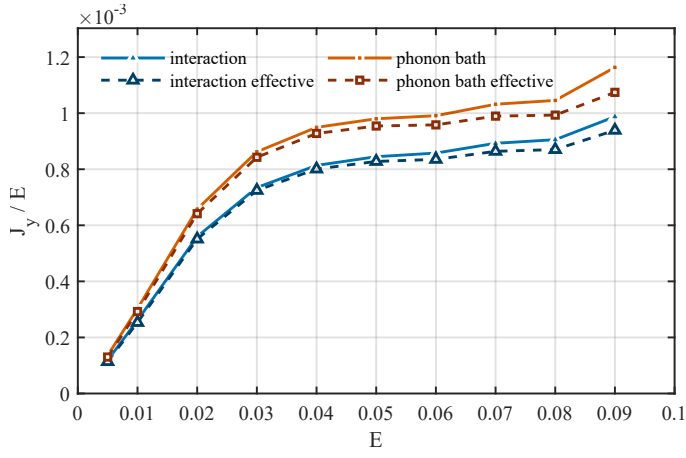


FIG. S11. Current response  $J_y/E$  as a function of electric field  $E$  for the model with electron-electron interactions and phonon-bath, respectively. Solid lines show the full calculation, while dashed lines show the corresponding effective descriptions with modified  $D_y$ .

is extracted from the zero-field self-energy using Eq. (S93). The resulting Hall responses are shown in Fig. S11. At relatively small fields, the effective- $D_y$  calculation reproduces the full electron-phonon and interaction results well. This confirms that the enhancement of the Hall response mainly originates from the real-part self-energy correction to the Berry-curvature distribution. At larger fields, deviations appear because the self-energy itself is modified by the driven nonequilibrium distribution and by the self-consistency of the full calculation. Nevertheless, the overall agreement demonstrates that the dominant effect of both electron-phonon coupling and local interactions in the present regime is the self-energy-induced modification of the low-energy band geometry, rather than a simple change of the scattering rate.